JOURNAL OF PETROLOGY

Journal of Petrology, 2016, Vol. 57, No. 11&12, 2289–2310
doi: 10.1093/petrology/egw065
Advance Access Publication Date: 24 December 2016
Original Article

OXFORD

The Composition of Melts from a Heterogeneous Mantle and the Origin of Ferropicrite: Application of a Thermodynamic Model

Eleanor S. Jennings*, Tim J. B. Holland, Oliver Shorttle†, John Maclennan and Sally A. Gibson

Department of Earth Sciences, University of Cambridge, Downing Street, Cambridge CB2 3EQ, UK

*Corresponding author. Present address: Bayerisches Geoinstitut, Universität Bayreuth, 95440 Bayreuth, Germany. E-mail: eleanor.jennings@uni-bayreuth.de
†Present address: Department of Geological and Planetary Sciences, California Institute of Technology, Pasadena, CA 91125, USA

Received December 3, 2015; Accepted October 13, 2016

ABSTRACT

Evidence for chemical and lithological heterogeneity in the Earth's convecting mantle is widely acknowledged, yet the major element signature imparted on mantle melts by this heterogeneity is still poorly resolved. In this study, a recent thermodynamic melting model is tested on a range of compositions that correspond to potential mantle lithologies (harzburgitic to pyroxenitic), to demonstrate its applicability over this compositional range, in particular for pyroxenite melting. Our results show that, despite the model's calibration in peridotitic systems, it effectively reproduces experimental partial melt compositions for both Si-deficient and Si-excess pyroxenites. Importantly, the model accurately predicts the presence of a free silica phase at high pressures in Si-excess pyroxenites, indicating the activation of the pyroxene–garnet thermal divide. This thermal divide has a dominant control on solidus temperature, melt productivity and partial melt composition. The model is used to make new inferences on the link between mantle composition and melting behaviour. In silica-deficient and low-pressure (olivine-bearing) lithologies, melt composition is not very sensitive to source composition. Linearly varying the source composition between peridotite and basaltic pyroxenite, we find that the concentration of oxides in the melt tends to be buffered by the increased stability of more fusible phases, causing partial melts of even highly fertile lithologies to be similar to those of peridotite. An exception to this behaviour is FeO, which is elevated in partial melts of silica-deficient pyroxenite even if the bulk composition does not have a high FeO content relative to peridotite. Melt Al_2O_3 and MgO vary predominantly as a function of melting depth rather than bulk composition. We have applied the thermodynamic model to test the hypothesis that Fe-rich mantle melts such as ferropicrites are derived by partial melting of Si-deficient pyroxenite at elevated mantle potential temperatures. We show that the conspicuously high FeO in ferropicrites at a given MgO content does not require a high-Fe mantle source and is indeed best matched by model results involving around 0–20% melting of silica-deficient pyroxenite. A pyroxenite source lithology also accounts for the low CaO content of ferropicrites, whereas their characteristic low Al_2O_3 is a function of their high pressure of formation. Phanerozoic ferropicrites are exclusively located in continental flood basalt (CFB) provinces and this model of formation confirms that lithological heterogeneity (perhaps recycled oceanic crust) is present in CFB mantle sources.

Key words: pyroxenite; eclogite; ferropicrite; mantle melting; mantle heterogeneity

INTRODUCTION

A thermodynamic approach to mantle heterogeneity

Subduction recycling may have operated over billions of years, continuously returning surface material to depth; consequently, the Earth's mantle is likely to be highly heterogeneous (Hofmann & White, 1982; Hofmann, 1997; Stracke, 2012). Melting and mixing of this recycled material over time may have resulted in the convecting mantle gaining a complex structure with a range of lithologies. Radiogenic isotopes in ocean island basalts (OIB) and mid-ocean ridge basalts (MORB) provide the clearest evidence for the presence of heterogeneity both in the MORB-source mantle and in the deeper mantle advected by plumes (Hofmann & White, 1982; Dupré & Allègre, 1983; Zindler & Hart, 1986; Hofmann, 1997). Moreover, the trace element characteristics of MORB and OIB associated with particular mantle end-members have been used to identify the sources and processes creating mantle heterogeneity, with basaltic oceanic crust, sediments, continental crust, and subcontinental lithospheric mantle all having been proposed as candidates for the identities of heterogeneities (Zindler & Hart, 1986; Weaver, 1991; Chauvel *et al.*, 1992; Hofmann, 1997; Gibson *et al.*, 2005; Willbold & Stracke, 2006; Jackson & Dasgupta, 2008; Kawabata *et al.*, 2011). Given the ubiquity and longevity of subduction recycling, oceanic lithosphere is commonly considered the most important potential source of heterogeneity in the convecting mantle (Stracke, 2012).

By comparison, the major element chemistry of mantle-derived melts is less frequently used to investigate the lithological and compositional heterogeneity of their mantle sources. Unlike trace elements and isotopes, major elements cannot be treated as passive tracers during melting. Rather, their abundance in the melt source region controls its mineralogy and melting relationships, making the prediction of the major element compositions of the partial melts more complex. Two approaches are generally employed: experimental petrology and thermodynamic calculations.

Experimental petrology has greatly improved our understanding of the behaviour of the mantle during melting and, together with a consideration of fractionation and transport processes, experiments on natural and synthetic peridotites have long been used to effectively explain the first-order features of basalt geochemistry (e.g. Yoder & Tilley, 1962; O'Hara, 1968; Green, 1973; Takahashi & Kushiro, 1983; Falloon & Green, 1987; Takahashi *et al.*, 1993). As it has become increasingly apparent that the mantle is lithologically heterogeneous, more recent experimental studies have focused on the melting behaviour of compositions that are richer in silica than typical mantle peridotite. These can be divided into two compositional groups according to their projection onto the Si-excess or Si-deficient side of the pyroxene–garnet compositional plane, which forms a thermal divide at high pressure (O'Hara & Yoder, 1967; O'Hara, 1968).

Si-excess compositions (referred to in this study as 'eclogite') contain a free silica phase at pressures above those at which the thermal divide becomes operational, which will dramatically change the melting behaviour (O'Hara & Yoder, 1967; Kogiso *et al.*, 2004). Eclogite is introduced into the convecting mantle as subducted oceanic crust (MORB), which undergoes chemical and metamorphic transformation (Green & Ringwood, 1967). Its partial melts have Fe- and Ca-poor, high-Si compositions, at least until quartz or coesite is lost from the melting assemblage (e.g. O'Hara, 1968; Pertermann & Hirschmann, 2003*a*; Kogiso *et al.*, 2004; Spandler *et al.*, 2008; Lambart *et al.*, 2013; Rosenthal *et al.*, 2014). However, in many locations, primitive erupted melts do not resemble these compositions (with notable exceptions such as the Koolau series in Hawai'i; Hauri, 1996; Herzberg, 2011). It has been shown through peridotite–basalt sandwich experiments that partial melts of eclogite will metasomatize surrounding peridotite to consume olivine and become silica-deficient pyroxenite (Yaxley & Green, 1998; Yaxley, 2000; Mallik & Dasgupta, 2012). The resultant pyroxenite is more fusible than peridotite and can partially melt to produce mafic–ultramafic liquids only subtly different from peridotite-derived melts (e.g. Lambart *et al.*, 2009). These pyroxenite partial melts and/or the reacted eclogite partial melts are often suggested to account for the major element features of some OIB and continental flood basalts (CFB), implying the presence of recycled eclogite or secondary pyroxenite in their source (e.g. Kogiso *et al.*, 1998, 2003; Gibson, 2002; Hirschmann *et al.*, 2003; Prytulak & Elliott, 2007; Dasgupta *et al.*, 2010; Herzberg, 2011; Mallik & Dasgupta, 2012).

Natural melts are not expected to perfectly match experimental ones because experiments tend to be isobaric and induce batch melting, whereas melt extraction is thought to be efficient in the mantle (Kelemen *et al.*, 1997). To access the low melt fractions (F) required to simulate fractional melting, as well as to extrapolate across P–T space and to bulk compositions (X) not directly interrogated by experiments, a thermodynamic model is required. Thermodynamic models are calibrated from experimental data and provide a flexible means to interpolate between, and extrapolate beyond experimental data points to explore a wider parameter space (P, T, F, X). Thus far, thermodynamic modelling predictions of melting of more enriched lithologies have been restricted to the pMELTS model, for which an upper pressure limit of 30 kbar is suggested (Ghiorso *et al.*, 2002). In this study, the new thermodynamic melting model in the eight-component NCFMASOCr system of Jennings & Holland (2015) is used to investigate the dependence of melt composition and productivity on bulk composition. Although the model used in this work was calibrated for peridotite melting, our findings demonstrate its effectiveness for more silica-rich compositions by means of reproducing

experimental run products from a range of bulk compositions. We use this model to assess the origin of Phanerozoic high-FeO primitive melts (i.e ferropicrites).

MELTING OF NON-LHERZOLITE MANTLE LITHOLOGIES: APPLICATION OF A THERMODYNAMIC MODEL

In this study we use the thermodynamic model of Jennings & Holland (2015), based on the dataset of Holland & Powell (2011), to investigate the major element compositions of melts derived from variable mantle compositions. The Jennings & Holland (2015) model adds an eight-component melt phase, as well as ferric and chrome end-members for solid phases, to the dataset of Holland & Powell (2011) and its more recent developments. The model is in the eight-component system NCFMASOCr, which is considered complex enough that it begins to approximate natural processes. For lherzolite, it is effective from 0 to 60 kbar and from 800°C to liquidus temperatures. The melt model was originally calibrated based on experimental studies of partial melting of fertile peridotite KLB-1 (Takahashi *et al.*, 1993), which is often used to approximate the composition of the upper mantle. The model is implemented in THERMOCALC (Powell *et al.*, 1998), includes a new melt phase, and can be effectively used to investigate mantle melting, including at near-solidus conditions.

Although the model of Jennings & Holland (2015) was calibrated for peridotite, the compositional range over which it is effective was not previously established. The purpose of such a thermodynamic model is to extrapolate from experimental results, and so its effectiveness for different bulk compositions can be assessed by its ability to reproduce experimental melt compositions, melt fractions and solid phase assemblages not included in the calibrating dataset. The following sections assess the applicability of the model to a range of bulk compositions corresponding to several potential mantle lithologies, and investigate their phase relations.

Silica-deficient pyroxenite

Silica-deficient pyroxenite (olivine-bearing or bimineralic) may form in the convecting mantle by a variety of mechanisms: solid-state reaction between eclogite and peridotite, and metasomatism of peridotite by Si-rich melts, are commonly suggested (e.g. Yaxley & Green, 1998; Kogiso *et al.*, 2004; Herzberg, 2011; Rosenthal *et al.*, 2014). Other possible origins may include subduction of lithospheric pyroxenite (Pilet *et al.*, 2005) or even the solid residue left after eclogite partial melting (Kogiso & Hirschmann, 2006; Rosenthal *et al.*, 2014). These varying pyroxenite formation mechanisms may lead to the presence of a broad range of pyroxenite compositions in the mantle, which is reflected in the diversity of starting compositions used in experimental studies [as reviewed by Lambart *et al.* (2013)]. For simplicity, the KG1 bulk composition of Kogiso *et al.* (1998) is examined here (Table 1). The KG1 composition is a 1:1 mixture of MORB and KLB-1 peridotite, which is high in MgO relative to most pyroxenite experimental starting compositions (see Lambart *et al.*, 2013). It is a hybrid peridotite–eclogite composition that captures the above processes to the first order, and experiments at a range of pressures and melt fractions have been published for this composition (Kogiso *et al.*, 1998). Although the physical setting that would allow such a material to be generated is not well understood, this bulk composition has been suggested as a putative lithology for the source regions of enriched Iceland basalts (Shorttle and Maclennan (2011)).

Two versions of the KG1 composition are used in this study: KG1(8) is the KG1 composition of Kogiso *et al.* (1998) normalized to 100% in the eight-component NCFMASOCr system with ferric iron content halfway between that of KLB-1 and MORB, whereas KG1(7) is normalized in the seven-component ferric iron-free system NCFMASCr (Table 1). The following calculations are performed on KG1(7) such that the results are comparable with the experiments of Kogiso *et al.* (1998), which were performed in graphite capsules.

To guide the calculation of liquid compositions and illuminate the phase relations of a silica-deficient pyroxenite, a *P*–*T* pseudosection for KG1(7) was constructed (Fig. 1). This pyroxenite has a similar topology and garnet–spinel transition to that of fertile peridotite KLB-1 (Jennings & Holland, 2015), although orthopyroxene is not stable along the pyroxenite solidus to as high pressure as on the KLB-1 solidus [orthopyroxene vanishes at around 18 kbar in KG1(7) and 42 kbar in KLB-1]. The spinel model used is rather simplified, and the spinel stability field predicted at high temperature may be an artefact (Jennings & Holland, 2015). The equilibrium isobaric liquid compositions at 15, 20 and 30 kbar are shown in Fig. 2, along with the experimental liquid compositions of Kogiso *et al.* (1998). Model temperatures at a given melt fraction are 20–60°C lower than experimental partial melts of KG1. This may indicate a model deficiency when performing calculations on more enriched compositions, but could also incorporate the uncertainty in determining melt fraction and temperature in experiments. The model melt compositions are similar to those formed in experiments, and in all cases the trends with *P* and *F* are matched (e.g. CaO increases with *F* and FeO increases with *P*). Some notable offsets exist, especially with the highest pressure experiments: at 30 kbar, the model melt has higher SiO_2 and FeO and lower MgO than the experimental melt compositions. However, both the model and experimental melts are subject to uncertainties. We suggest that, because the model acceptably reproduces liquid compositions within typical experimental tolerance and achieves the same sense of change with pressure, it may be used for predicting partial melts in bulk compositions similar to KG1.

Table 1: Bulk compositions: published version (with reference) and the seven- or eight-component version used in this study

	Published compositions				Compositions used in this study						
	KLB-1 (Davis *et al.*, 2009)	KG1 (Kogiso *et al.*, 1998)	G2 (Pertermann & Hirschmann, 2003*a*)	N-MORB (Gale *et al.*, 2013)	Depleted peridotite $X=-0{\cdot}1$	KLB-1 $X=0$	KG1(7)	KG1(8) $X=0{\cdot}5$	G2(7)	G2(8)	N-MORB $X=1$
SiO_2	44·84	46·97	50·05	50·47	44·14	45·65	47·4	48·72	51·11	50·13	51·86
TiO_2	0·11	0·78	1·97	1·64							
Al_2O_3	3·51	9·75	15·76	14·84	2·2	2·53	9·84	9·85	16·1	15·79	15·11
FeO*	*8·20*	*9·77*	*9·35*	*10·19*	7·86	8·01	9·86	8·38	9·55	9·36	8·74
Fe_2O_3					0·12	0·29		1·15		1·92	1·85
MnO	0·12		0·19	0·18							
MgO	39·52	23·57	7·90	7·66	43·23	39·83	23·78	22·23	8·07	7·91	7·79
CaO	3·07	7·35	11·74	11·43	2·09	3·13	7·42	7·79	11·99	11·76	11·71
Na_2O	0·30	1·52	3·04	2·83	0·01	0·31	1·53	1·7	3·1	3·05	2·87
K_2O	0·02	0·12	0·03	0·16							
Cr_2O_3	0·32	0·17		0·04	0·35	0·26	0·17	0·18	0·08	0·08	0·07

The seven- or eight-component version of bulk compositions is the published version with extra components subtracted and normalized to total 100%, with or without Fe^{3+}. *X* denotes position along a compositional vector where zero is KLB-1 and unity is N-MORB. Concentrations are given in wt. % oxide.
*FeO_{Total} for italicized values (Fe^{3+}/Fe_{Total} not measured but assumed insignificant in experiments performed in graphite capsules).

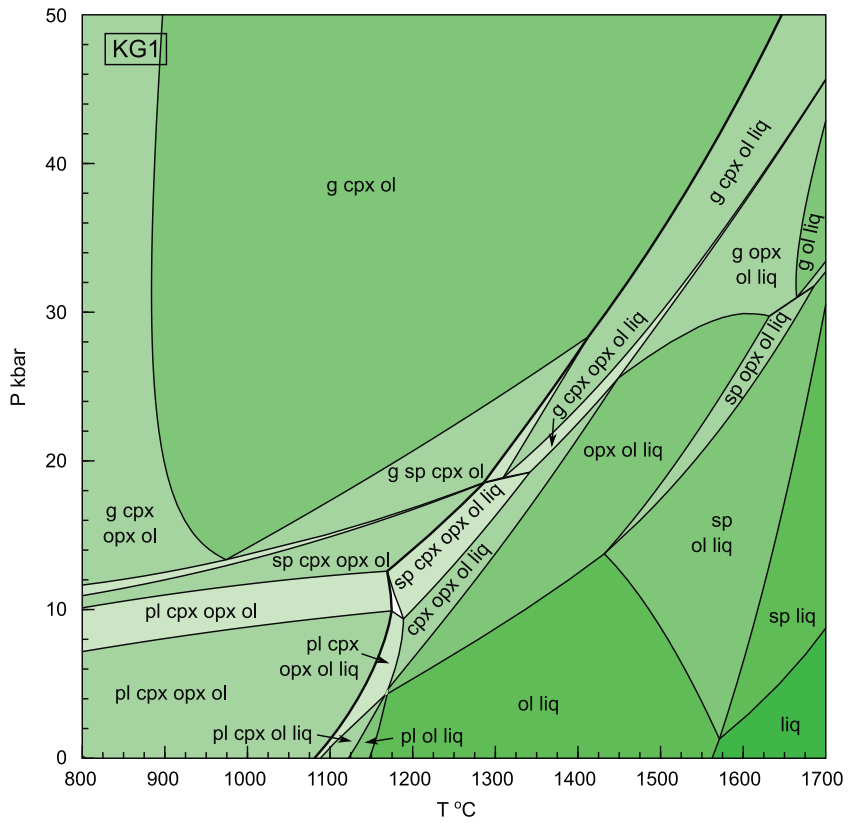

Fig. 1. *P–T* pseudosection for the bulk composition of hypothetical pyroxenite KG1(7) in the NCFMASCr system (bulk composition given in Table 1). Phases: g, garnet; sp, spinel; pl, plagioclase; ol, olivine; cpx, clinopyroxene; opx, orthopyroxene; liq, liquid. Darker fields are higher variance. It should be noted that the spinel stability fields near the liquidus contains <1 wt % spinel, which may be an artefact.

For comparison, a similar calculation was performed in pMELTS (pMELTS is not optimized for pyroxenite melting). These calculations use the same KG1 bulk composition with the addition of the published TiO_2 content (Kogiso *et al.*, 1998) at QFM – 3 (where QFM is the quartz–fayalite–magnetite buffer), with results normalized in the eight-component NCFMASOCr system. The resulting liquid compositions are overlain on a version of Fig. 2 in Supplementary Data Fig. 1 (supplementary data are available for downloading at http://www.petrology.oxfordjournals.org); pMELTS does not effectively predict the experimental melt compositions

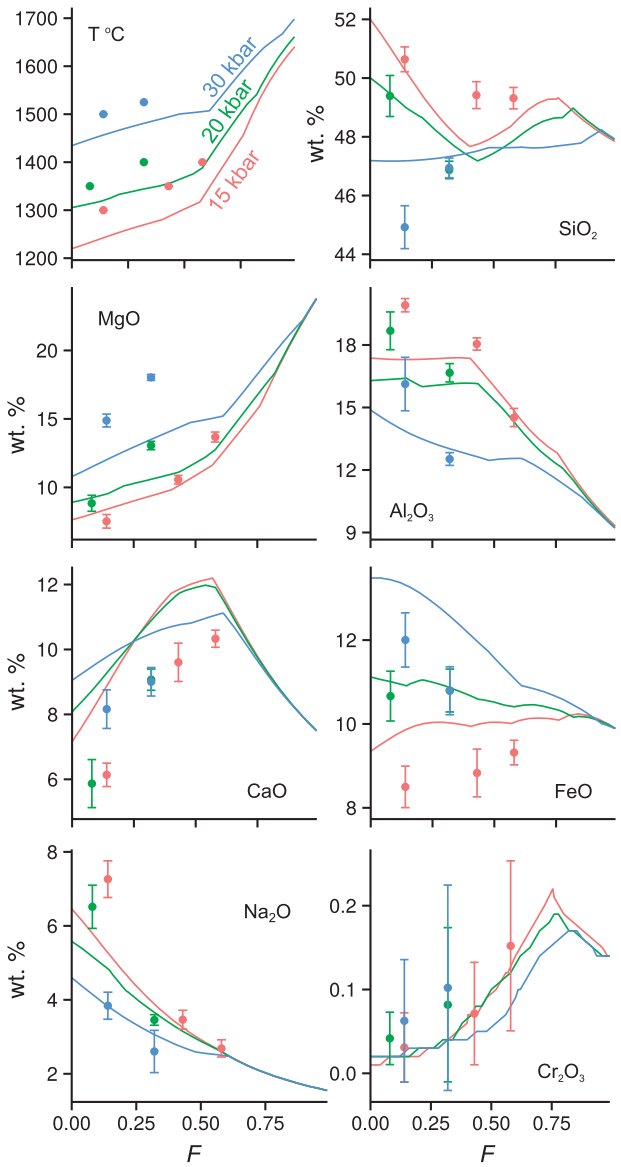

Fig. 2. Comparison of model melt compositions (lines) with the experimental melts of Kogiso *et al.* (1998) (points). For the model melts, the ferric iron-free KG1(7) composition was used (Table 1). Ferric iron was not included to reflect the reducing conditions in the experimental charges. Red, 15 kbar; green, 20 kbar; blue, 30 kbar. Experimental melt compositions are normalized to 100% in the same seven-component system. (See Supplementary Data, Fig. 1 for pMELTS results overlay.)

of Kogiso *et al.* (1998) for most oxides. Although pMELTS performed better than the present model for CaO and produced acceptable results for some oxides at 15 kbar, it was particularly poor at 30 kbar and in Al_2O_3, FeO and SiO_2, and is thus not further used in the present study.

Silica-excess eclogite

Two bulk compositions are examined by calculating their *P–T* pseudosections (Fig. 3): (1) average normal (N-)MORB of Gale *et al.* (2013); (2) G2, an eclogite in the middle of the natural sample array (Pertermann & Hirschmann, 2003*a*). These pseudosections are calculated with $Fe^{3+}/Fe_T = 0{\cdot}16$ in the bulk composition, after Cottrell & Kelley (2011), where bulk compositions are normalized in the eight-component system [compositions N-MORB and G2(8) of Table 1]. The figures show that, in contrast to fertile peridotite and silica-deficient pyroxenite, olivine is present on the solidus only at low pressure (<7–8 kbar) in both compositions. Above this pressure, an olivine- and quartz-free interval exists until quartz joins the solidus assemblage at 13 and 18 kbar for N-MORB and G2(8), respectively. G2(8) contains 1·5 mol % less SiO_2 than average MORB, resulting in the low-pressure quartz stability limit on the solidus occurring at higher pressure. In both compositions, garnet appears on the solidus at around 15 kbar and a small mode of kyanite is stabilized over 25 kbar. This change in subsolidus assemblage with increasing pressure represents the activation of the thermal divide at the pyroxene–garnet join. The reactions that cause the disappearance of some phases (olivine and plagioclase) and the appearance of others (garnet and quartz) are univariant in *P–T* space in the simple CMAS system (O'Hara, 1968), whereas they are multivariant in the present eight-component NCFMASOCr system. This change in assemblage causes a prominent bulge on the solidus between the pressures of the olivine-out and quartz-in boundaries as melting moves from the olivine-bearing eutectic to the quartz-bearing one.

The effect of the different solidus phase assemblages on the partial melt compositions of G2 is seen in Fig. 4. For this calculation, the ferric iron-free bulk composition G2(7) was used to reflect the experimental conditions (Table 1). The G2 and G2K experimental melt compositions of Pertermann & Hirschmann (2003*a*), and other experimental melt compositions (12·5–50 kbar) from similar volatile-free basalt and eclogite-like bulk compositions (Takahashi *et al.*, 1998; Yaxley & Green, 1998; Takahashi & Nakajima, 2002; Yaxley & Sobolev, 2007; Spandler *et al.*, 2008; Rosenthal *et al.*, 2014), are shown for comparison. During isobaric melting of G2(7) at 20 kbar, quartz is lost at very low melt fraction ($F \sim 0$) from the melting assemblage. However, by 30 kbar quartz stability is increased and is present to $F = 0{\cdot}14$; this is also true of the observed melting assemblages of Pertermann & Hirschmann (2003*a*). This leads to a significant difference in the partial melt compositions between the two pressures, and melts at the quartz-present eutectic (30 kbar) have much higher SiO_2 and lower FeO than those generated by melting of the effectively quartz-free assemblage. At melt fractions above 0·14, where quartz is exhausted from the high-pressure assemblage, the melt compositions at the two pressures converge. The two low-fraction melting behaviours (quartz-bearing and quartz-absent) could account for some of the range in melt SiO_2, CaO, FeO and Al_2O_3 produced in the other experimental studies shown, although most experimental datapoints roughly follow the initially quartz-bearing trend. Other sources of variability in the experimental database are the

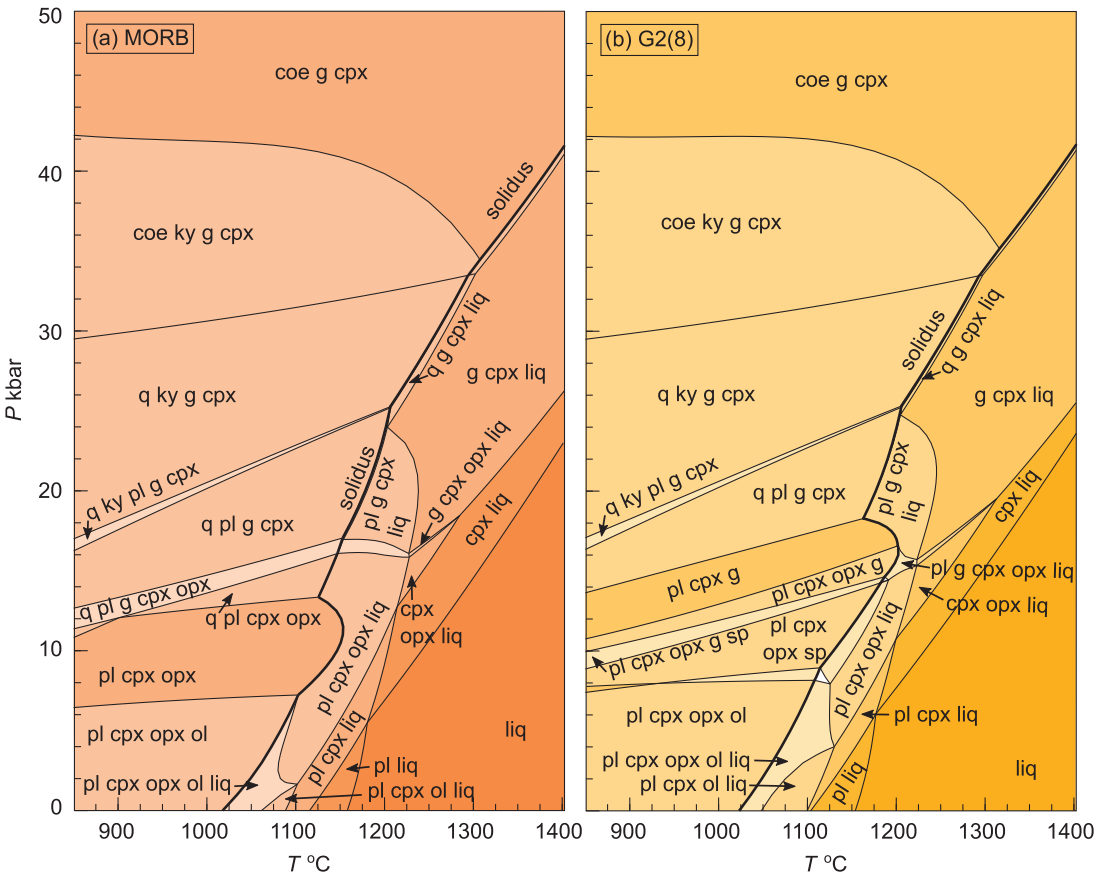

Fig. 3. *P–T* pseudosection calculated for (a) average MORB bulk composition of Gale *et al.* (2013) (N-MORB, Table 1) and (b) G2(8) eclogite bulk composition [Table 1; after G2 composition of Pertermann & Hirschmann (2003*a*)], both in the NCFMASOCr system with $Fe^{3+}/Fe_T = 0{\cdot}16$ (after Cottrell & Kelley, 2011). Legend as for Fig. 1; additional phases: q, quartz; coe, coesite; ky, kyanite. Spinel is not present in (a).

differing bulk composition and pressures used. Interestingly, the low-*F* experimental melts of Pertermann & Hirschmann (2003*a*) at 30 kbar better match the quartz-absent melting behaviour in the model observed at 20 kbar, despite quartz being reported in the experimental residue. G2K is a bulk composition containing somewhat higher K_2O and SiO_2 than G2, and gives experimental melt compositions that are more similar to the quartz-residue (30 kbar) modelled ones. Given the lack of K_2O in the present model, we suggest that the better fit of G2K to the model results is explained by the extra SiO_2 stabilizing quartz in the experiments.

Overall, the model produces an acceptable fit to the experimental data at melt fractions above that of quartz exhaustion, and the range of experimental compositions can be largely explained by the presence or absence of residual quartz in the melting assemblage.

Depleted peridotite

Finally, a bulk composition more depleted than KLB-1 is considered. Depletion of a peridotite by partial melting will preferentially exhaust clinopyroxene and the relevant aluminous phase. Around 20% partial melting will remove all clinopyroxene from the KLB-1 residue (Jennings & Holland, 2015). In this study, a depleted peridotite composition is created by subtracting 10% of average N-MORB from the composition of KLB-1 (see Table 1). The resultant depleted peridotite composition contains 0·01 wt % Na_2O and corresponds to a clinopyroxene-bearing harzburgite at subsolidus *P–T* conditions. Its *P–T* pseudosection (Fig. 5) is very similar to that of KLB-1 (Jennings & Holland, 2015) but with orthopyroxene remaining present on the solidus to pressures of hpx stability (high-pressure pyroxene; Holland *et al.*, 2013). Wasylenki *et al.* (2003) performed melting experiments on a depleted upper mantle composition (DMM1), which contained a small fraction of clinopyroxene lost at $F = 0{\cdot}1$. The lower fraction melt compositions of DMM1 were very similar to higher fraction melts of KLB-1 (except in the more incompatible elements such as Na_2O). Melting more depleted bulk compositions, where clinopyroxene is not present on the solidus, would create melts with similar compositions to higher fraction melts of KLB-1. As the current model functions well for high-fraction melts of KLB-1, it

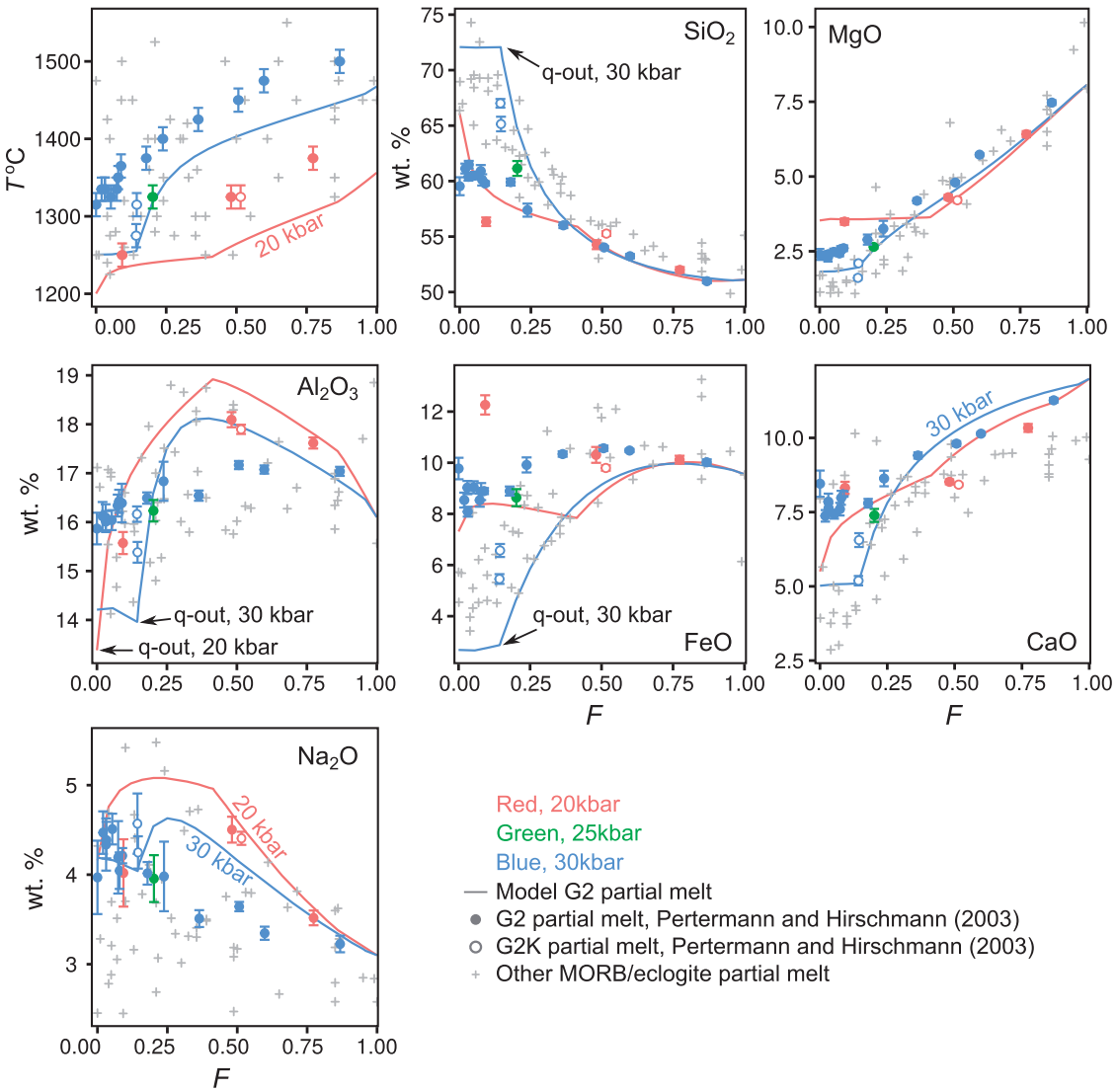

Fig. 4. Comparison of model melt compositions [lines, bulk composition G2(7)] with experiments of Pertermann & Hirschmann (2003*a*) (circles) for bulk composition G2 (experimental melts of G2K are also shown, which is a bulk composition somewhat higher in K_2O and SiO_2 than G2). Red, experiments and model at 20 kbar; green, 25 kbar; blue, 30 kbar. Experimental compositions and uncertainties are from Pertermann & Hirschmann (2003*a*). The G2(7) bulk composition is ferric iron-free for comparability with experiments, which are buffered by graphite (see Table 1). q-out marks the exhaustion of quartz from the solid. Large differences in melt compositions at low *F* are explained by the presence or absence of quartz. Experimental melts from other studies using anhydrous eclogite compositions at a range of pressures are shown with grey crosses (Takahashi *et al.*, 1998; Yaxley & Green, 1998; Takahashi & Nakajima, 2002; Yaxley & Sobolev, 2007; Spandler *et al.*, 2008; Rosenthal *et al.*, 2014).

is assumed that this will also be the case for depleted peridotite compositions.

RESULTS: THE EFFECTS OF VARYING MANTLE BULK COMPOSITION ON MANTLE MELTING

The melt model should be effective for mantle compositions ranging from depleted peridotite to MORB-like eclogite, so it can be used to explore the control of bulk composition on melt chemistry. To simplify this, the bulk compositions are conveniently chosen to be linear combinations of fertile peridotite KLB-1 ($X=0$; Davis *et al.*, 2009) and average N-MORB ($X=1$; Gale *et al.*, 2013), both normalized to 100% in the NCFMASOCr system, with Fe_2O_3 calculated by taking $Fe^{3+}/Fe_T=0{\cdot}03$ for KLB-1 and 0·16 for MORB, after Canil *et al.* (1994) and Cottrell & Kelley (2011), respectively. This binary join is illustrated in Fig. 6. As basalt (approximated by average MORB) is extracted from a primitive mantle lherzolite (KLB-1), the lherzolite bulk composition loses basalt and moves to negative *X*. Conversely, if average MORB is added to peridotite in some proportion through subduction, the mantle moves to positive *X*. This approximation reflects natural mafic–ultramafic rock systematics to a first order and allows a continuous range of potential mantle compositions to be investigated. In reality, this system does not account for the subtleties of fractional melting and melt mixing, crystal

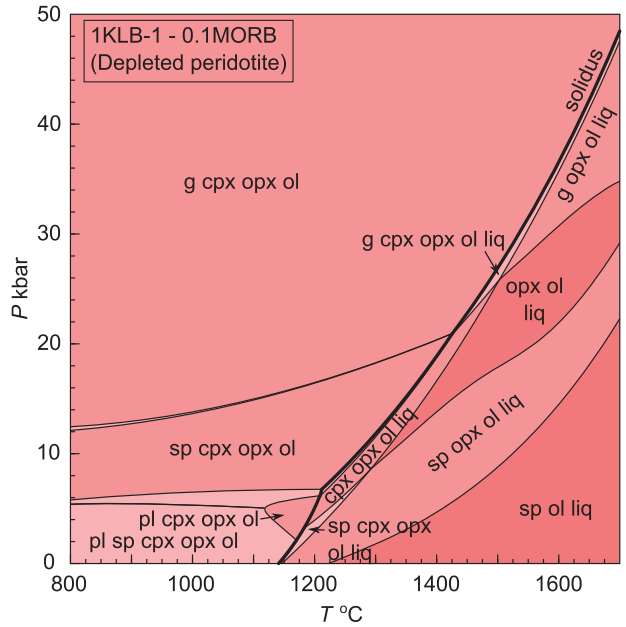

Fig. 5. *P–T* pseudosection for the depleted peridotite bulk composition $X = -0{\cdot}1$ (KLB-1 – 0·1 N-MORB), in the NCFMASOCr system. Phase labels and legend as for Fig. 1.

fractionation, and MORB modification by subduction zone processes.

Solidus phase assemblage

Knowledge of the solidus phase assemblage is important for understanding the trace element geochemistry of mantle melts, as well as for predicting their major element composition. Phase assemblages at the solidus for various pressures as a function of composition are shown in Fig. 7. The pyroxene–garnet compositional plane is crossed at around $X = 0{\cdot}70$, above which quartz replaces olivine on the solidus in higher pressure assemblages. In detail, the thermal divide is multivariant in the present system: at 22 kbar a narrow interval exists between $X = 0{\cdot}68$ and $X = 0{\cdot}70$ where neither olivine nor quartz is present, and at 50 kbar this region shifts to $X = 0{\cdot}71$–$0{\cdot}72$. Plagioclase is stable in more basalt-rich compositions to higher pressures on the solidus, whereas orthopyroxene is stable to the highest pressures in the most depleted compositions. Although

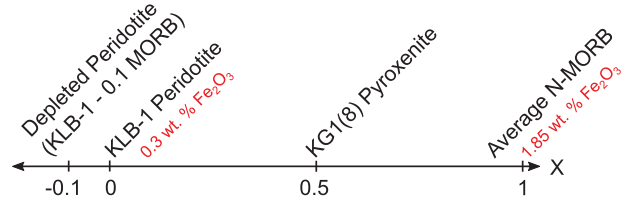

Fig. 6. Illustration of the binary compositional range described by the compositional parameter X, where $X = 0$ is the enriched peridotite KLB-1 (Davis *et al.*, 2009, with 0·3 wt % Fe_2O_3, Canil *et al.*, 1994), and $X = 1$ is average N-MORB (Gale *et al.*, 2013, with 1·85 wt % Fe_2O_3, Cottrell & Kelley, 2011). Other X values are linear combinations of KLB-1 and MORB, where $X = 0{\cdot}5$ [KG1(8)] is very similar to pyroxenite KG1 of Kogiso *et al.* (1998). Compositions are listed in Table 1.

the various *P–T* pseudosections presented here and by Jennings & Holland (2015) indicate that the lower pressure limit for garnet stability is moderately insensitive to bulk composition, it is seen here that the modal proportion of garnet in high-pressure assemblages (50 kbar) increases from just 5% in harzburgite to 40% in average MORB. Pyroxenite KG1(8) ($X = 0{\cdot}5$) contains 29% modal olivine at 5 kbar, decreasing to 11% at 50 kbar, making this composition an olivine websterite or olivine clinopyroxenite, depending on pressure.

Thermal properties: solidus and melt productivity

Experimental determinations of the onset of melting in various compositions indicate that pyroxenite should begin to melt at somewhat lower temperature (or higher pressure) than peridotite, and eclogite at lower temperature still (Yasuda *et al.*, 1994; Kogiso *et al.*, 1998; Yaxley & Green, 1998; Herzberg *et al.*, 2000; Hirschmann, 2000; Pertermann & Hirschmann, 2003*a*). A more important difference from peridotite is the melt productivity; that is, the amount of melting achieved over a given temperature interval below the liquidus. This is proposed to be much higher in pyroxenites, meaning that pyroxenite would melt to a greater extent over a given finite temperature increase or interval of isentropic decompression than would peridotite. Accumulated melts from a mixed lithology mantle would therefore be heavily biased towards originating from the more fusible lithology (Hirschmann & Stolper, 1996; Phipps Morgan, 2001; Kogiso *et al.*, 2004; Lambart *et al.*, 2013; Sims *et al.*, 2013; Shorttle *et al.*, 2014). The effect of the high-pressure pyroxene–garnet thermal divide on the solidus temperature is not fully resolved in complex systems (e.g. Kogiso *et al.*, 2004). It should be noted that, because natural mantle rocks contain volatile components, they may begin to produce incipient melts of volatile-rich composition much deeper than the onset of the high-productivity anhydrous peridotite melting (e.g. Dasgupta & Hirschmann, 2007). The compositions examined here are volatile- and potassium-free, so the calculated solidus represents the onset of this main phase of melting in natural samples, rather than the temperature at which they produce incipient melts.

The calculated solidus temperature for a continuous range of compositions at four pressures is shown in Fig. 8. At low pressures (5 and 13 kbar) across the full compositional range the solidus temperature is not very sensitive to bulk composition: an increase in basalt content only slightly lowers the solidus temperature. Between $X = 0$ (KLB-1 peridotite) and $X = 0{\cdot}5$ [KG1(8) silica-undersaturated pyroxenite], there is almost no difference in the solidus temperature. However, at the higher pressures, a free-silica phase is stabilized in the silica-excess ($X > 0{\cdot}70$) compositions. The quartz- or coesite-bearing eutectic is on the Si-rich side of the thermal divide, whereas the spinel ± olivine-bearing one is

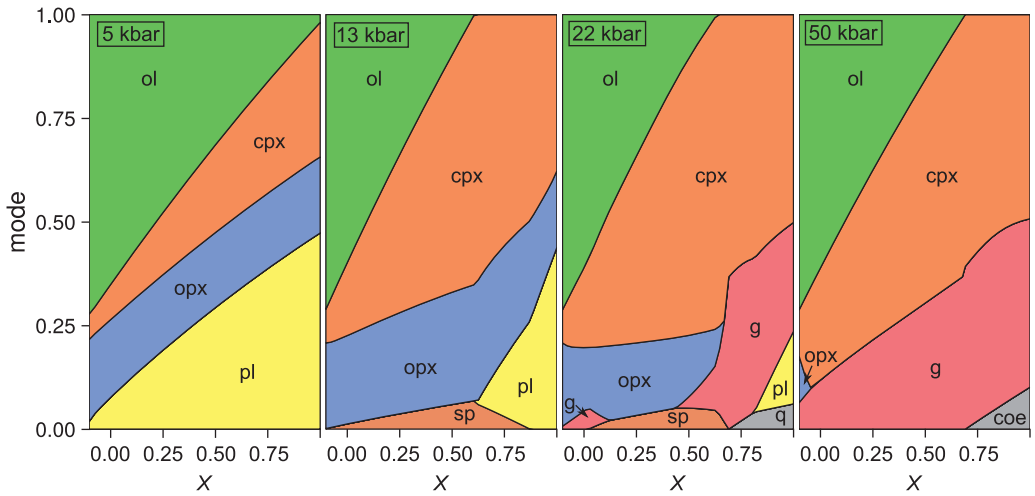

Fig. 7. Solidus modes (normalized to one oxide molar, similar to volume per cent) as a function of composition (*X*; see Fig. 6) for four pressures. Phase labels as in previous figures. The appearance of garnet twice at 22 kbar is a result of the narrow [g + sp] stability field moving slightly up in pressure, and then down again, with increasing *X*.

on the Si-poor side; thus, the thermal divide has become effective at this point. This new eutectic temperature is around 150°C lower, explaining the large drop in solidus temperature in higher pressure silica-excess compositions. This large discontinuity in solidus temperature is contrary to the suggestion of Kogiso *et al.* (2004) that subsolidus phase assemblages do not have an obvious influence on solidus temperatures, and means that subducted MORB-eclogite would indeed begin to melt much deeper than other mantle lithologies in upwelling plumes. However, during fractional melting, this deeper melting may be self-limiting: after the free-silica phase is exhausted (at around 0–20% melting, depending on pressure and bulk composition) melting will cease, and it restart only once the quartz-free solidus is reached.

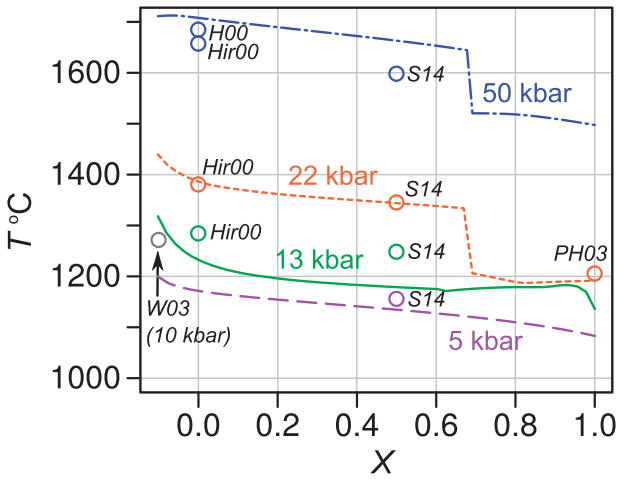

Fig. 8. Solidus temperature as a function of composition (*X*; see Fig. 6) and pressure. Line pattern and colour indicate pressure (purple, 5 kbar; green, 13 kbar; orange, 22 kbar; blue, 50 kbar). Also shown are experimental solidi (W03, at 10 kbar) or solidi calculated from published empirical parameterizations of experiments (remaining points), for compositions that fall on, or close to, the *X* binary join. References: W03, Wasylenki *et al.* (2003, DMM1); S14, Shorttle *et al.* (2014, KG1); H00, Herzberg *et al.* (2000, KLB-1); Hir00, Hirschmann (2000, various peridotites); PH03, Pertermann & Hirschmann (2003*b*, G2). Solidi from these parameterizations are calculated at 5, 13, 22 and/or 50 kbar, depending on the published calibration range (if any). The jump in solidus at high pressure is caused by the presence of quartz in the solidus assemblage at $X > 0{\cdot}69$.

Although olivine-bearing pyroxenites with compositions similar to KG1(8) do not have a solidus temperature that is particularly offset from that of fertile peridotite, their melt productivity contrasts strongly. The isobaric melt fraction as a function of temperature for four compositions is shown in Fig. 9. The contrasting behaviour is clear at 25 kbar (Fig. 9a). All compositions have a steep dF/dT slope until clinopyroxene exhaustion, and then switch to a lower productivity regime. In the fertile KLB-1 and depleted peridotite compositions, clinopyroxene is lost early and thus most of the melt fraction range is low productivity. This contrasts with MORB and KG1(8), which have steeper slopes at the onset of melting and lose clinopyroxene only after high-fraction melting, meaning that they will melt to a greater extent over a given temperature interval. At 25 kbar, KG1(8) has a solidus 50°C lower than that of KLB-1 (Fig. 9a). If melting were isobaric, by the onset of KLB-1 fertile peridotite melting the KG1(8) pyroxenite would be 50°C below its solidus and would already have melted by 50%, and N-MORB would be fully molten (in decompression melting, the effect of parameters such as the difference in entropy of fusion on the P–T path of the solid must be accounted for). At the onset of melting, MORB melt productivity is even more extreme until the loss of quartz from the residue. The same is true at 50 kbar (Fig. 9b). The solidus temperature projected along an adiabat and calculated without melting at the pressure of interest is also shown in Fig. 9; this indicates that at ambient T_P (1315°C) at 25 kbar only N-MORB will have begun to melt, whereas at $T_P = 1500$°C all compositions will have crossed their solidi.

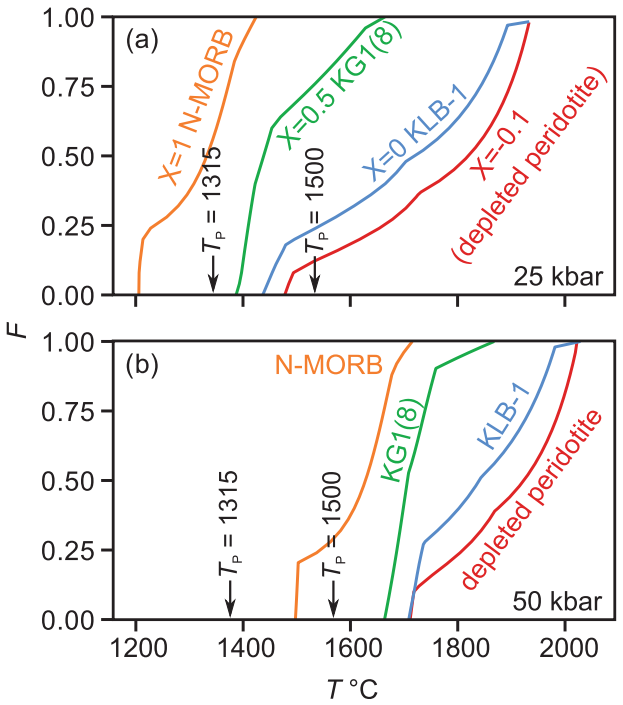

Fig. 9. Melt fraction (F) as a function of temperature at (a) 25 kbar and (b) 50 kbar. Orange, average MORB ($X=1$); green, pyroxenite KG1(8) ($X=0{\cdot}5$); blue, peridotite KLB-1 ($X=0$); red, depleted peridotite ($X=-0{\cdot}1$). Arrows indicate the mantle temperature, where potential temperature T_P is 1315°C and 1500°C, at the given pressure.

In a plume with mixed lithologies in thermal equilibrium, heat flow from unmelted refractory domains will further increase the isentropic melt productivity of the more fusible lithology (Sleep, 1984; Phipps Morgan, 2001).

Near-solidus melt compositions

The compositions of a nominal 0% melt fraction along the solidus as a function of bulk composition are shown in Fig. 10 at 5, 13, 22 and 50 kbar, along with the respective bulk compositions. Because the solidus temperature increases with pressure, higher pressure calculations represent the effect of increased depth of melting. For compositions that do not contain a free silica phase (i.e. all compositions at pressures of 5 and 13 kbar and compositions of $X<0{\cdot}70$ at higher pressures), compositional changes in the melt are muted relative to the change in bulk composition for most oxides. For example, for MgO, CaO and Al_2O_3 the melt composition is almost constant over a broad compositional range. These oxides are buffered by the residual mineral assemblage, as increases or decreases in the bulk composition change the modal proportions of minerals but have a limited effect on the melting reaction. CaO shows the opposite sense of change, where increasing bulk CaO is matched by a slight reduction in CaO of the low-fraction partial melt. This behaviour is in agreement with the observations of Herzberg (2011) and stems from the increased stability of clinopyroxene in more enriched compositions and its decreased contribution in the melting reaction relative to its mode. This leads to peridotite and pyroxenite partial melts being broadly similar, as has also been observed from experimental results (Lambart *et al.*, 2013). The exception to this behaviour is FeO, where the melt experiences a much larger change for more enriched compositions, despite the bulk FeO content remaining almost constant. This indicates that FeO may be a useful marker oxide in identifying melts from recycled lithologies (e.g. Kogiso *et al.*, 1998; Gibson, 2002; Shorttle and Maclennan (2011); Lambart *et al.*, 2013). This behaviour can be explained by considering the need for the melt and solid phases to maintain $K_D^{Fe–Mg}$ equilibrium: as the MORB component is added to the bulk composition, the MgO of the solid dramatically decreases, whereas the decrease in melt MgO is rather small (when considering melting of quartz-free assemblages). Because bulk MgO is much lower in MORB than in peridotite, and because the bulk FeO is roughly constant, melt FeO must increase to maintain $K_D^{Fe–Mg}$ equilibrium. This mechanism allows a partial melt to have elevated FeO without requiring an Fe-rich source.

For many oxides, the difference in melt composition caused by changing the depth of melting is greater than that caused by bulk compositional changes. Al_2O_3, MgO and Na_2O clearly demonstrate this, and can be explained in terms of changing phase composition and melting reactions (or phase stability) with depth. For example, MgO in melts increases with pressure as garnet and clinopyroxene stabilize at the expense of olivine (O'Hara, 1968), whereas Na_2O decreases with pressure above plagioclase-out as it becomes increasingly more compatible in clinopyroxene (Blundy *et al.*, 1995). The depth and compositional effects are somewhat convoluted in pyroxenite vs peridotite melting, as pyroxenites will both melt at higher pressures and have more enriched compositions.

In contrast to silica-deficient pyroxenites, quartz-bearing MORB-rich compositions begin to melt on the Si-excess side of the thermal divide at high pressures. The effect of this switch in the eutectic position for the SiO_2 and FeO content of melts is dramatic. The equilibrium melt compositions are significantly different from those of silica-deficient pyroxenites until quartz is exhausted from the residue. These early dacitic liquids are unlikely to reach the surface: they would form deep, are far from equilibrium with peridotite, and have a high viscosity.

Natural mantle melts represent higher fraction melting than incipient melts. Given that high-degree mantle melting is likely to be near-fractional, higher fraction melts can be approximated from Fig. 10 by assuming that the solid residue depletes to lower X as basalt is removed, obtaining subsequent instantaneous melt compositions, and considering that the final melt composition will be an average, mixed composition. In the case of pure batch melting, systematics can be gleaned from Figs 2 and 4.

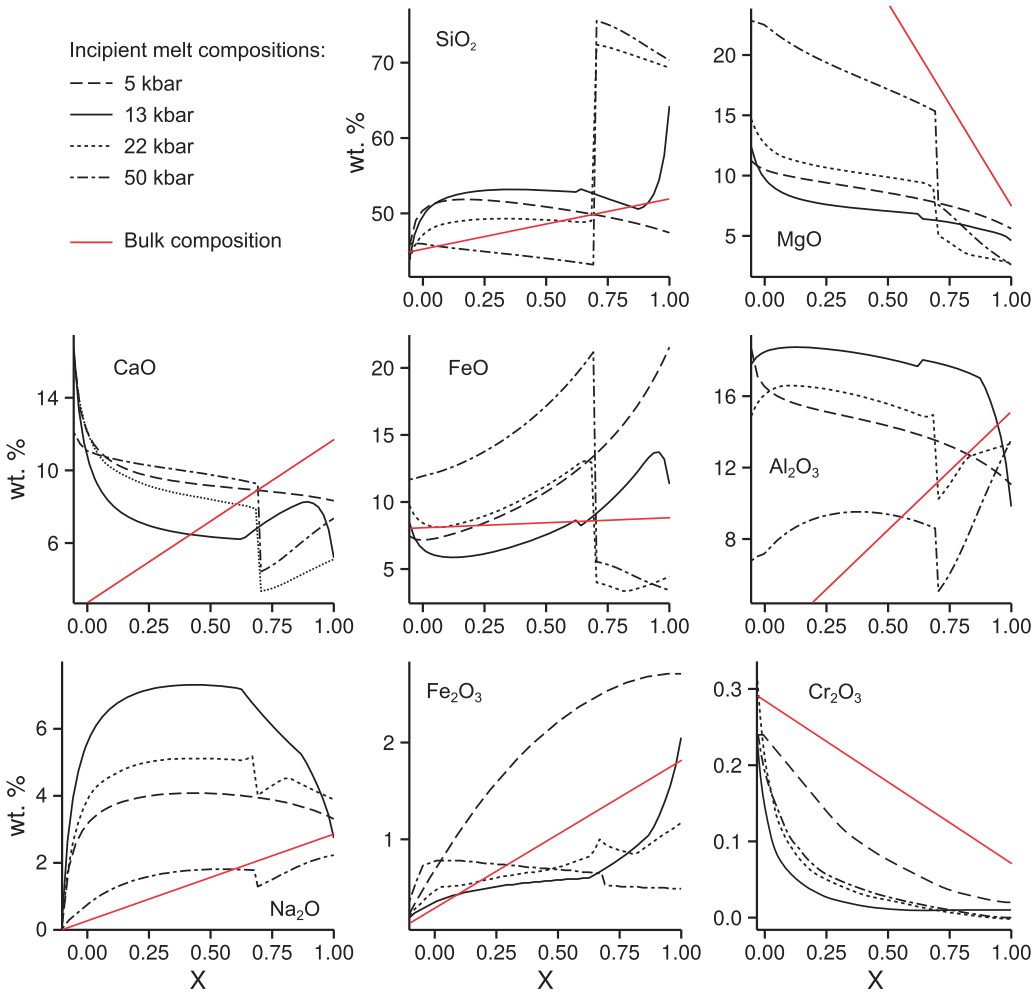

Fig. 10. Calculated solidus melt composition for a nominal zero melt fraction as a function of bulk composition *X* (from depleted peridotite through to eclogite) at 5, 13, 22 and 50 kbar.

DISCUSSION

The origin of mantle pyroxenite

The model of Yaxley & Green (1998), and later Sobolev *et al.* (2005), describes a two-stage process whereby: (1) eclogite partially melts at depth, and then (2) these partial melts metasomatize the surrounding peridotite to create pyroxenite, which itself melts deeper than peridotite. The composition of the resultant hybrid pyroxenite depends on the melt-to-rock ratio, the composition of the eclogite and peridotite, and the extent of melting. This process is consistent with the solidus pressures and melt productivities found in this study, although it is critically controlled by the ability of the high-silica melts to flow from their source. Melt–rock reaction between the eclogite partial melt and surrounding peridotite may precipitate pyroxene, reducing porosity and restricting the volume of peridotite that can become metasomatized (e.g. Mallik & Dasgupta, 2012; Rosenthal *et al.*, 2014).

During fractional melting (i.e. if the melt is able to escape the solid), eclogite will stop melting once the free silica phase is consumed. The solid residue that is left behind will lie close to the pyroxene–garnet compositional divide ($X = 0{\cdot}70$). At 30 kbar, G2(7) loses all of its quartz by $F = 0{\cdot}14$ in equilibrium melting, or at lower F in fractional melting. If the $F = 0{\cdot}14$ equilibrium dacitic melt is extracted, the residual solid is 48 wt % SiO_2, 9 wt % MgO, 11 wt % FeO, 16 wt % Al_2O_3 and 13 wt % CaO. This composition is low in MgO and high in Al_2O_3 compared with pyroxenite KG1 (22 wt % MgO, 10 wt % Al_2O_3) but is more similar to pyroxenite MIX1G (17 wt % MgO, 15 wt % Al_2O_3, 12 wt % CaO; Hirschmann *et al.*, 2003), which was created as an intermediate composition within the natural mantle pyroxenite array. The melting residue of mantle eclogite could therefore also be considered as a pyroxenite source for melts, although such melts may be depleted in highly incompatible trace elements. Because pyroxenite and eclogite melt more productively than peridotite, an accumulated magma from partial melting of a lithologically heterogeneous mantle will reflect a greater contribution of melt from the more fusible lithologies, in agreement with

previous understanding (e.g. Hirschmann & Stolper, 1996; Shorttle *et al.*, 2014).

Fractional melting simulations

Mantle melting is near-fractional and polybaric, meaning that the resultant aggregated melt compositions will differ from the equilibrium compositions identified in Figs 2, 4 and 10. Fractional melting simulations were therefore performed to investigate the melt compositions expected from peridotite and pyroxenite partial melting in an isentropically decompressing mantle. The results of these simulations (incremental melt compositions) are provided in Supplementary Data Table 1.

Thermal structure

It is not possible to calculate self-consistent isentropic decompression paths in THERMOCALC so a *P*–*T* path must be independently calculated and imposed (compare the MELTS family of models and associated software; Ghiorso & Sack, 1995; Smith & Asimow, 2005). A stepwise equilibrium melting regime is used, where melt is extracted at a threshold fraction; these incremental melts are integrated in a one-dimensional (1D) geometry for a final mixed melt composition. At every step, the bulk composition is recalculated by removing the previous melt. A melt fraction step of $F = 0{\cdot}01$ was found to be an appropriate compromise between resolution and time efficiency (a repeat of a calculation run for KLB-1 at $F = 0{\cdot}005$ resulted in almost identical integrated compositions at a given melt fraction). An accumulated stepped melting approach is broadly consistent with the idea that mantle melting may require a residual or threshold porosity for melt extraction to occur, although U-series disequilibrium suggests that porosities may be small, assuming a peridotite source [reviewed by Kelemen *et al.* (1997)].

Melting at ambient mantle T_P will begin at shallower pressures than melting at elevated T_P, and shows the melt compositions expected from passive upwelling in rift scenarios. For plume-type active upwelling, T_P is used as a general representation of the effect of elevated temperature, and therefore deeper melting. $T_P = 1500^\circ$C is broadly applicable to many known plumes given the uncertainties associated with making mantle temperature estimates (Herzberg *et al.*, 2007; Putirka *et al.*, 2007). Four scenarios were therefore modelled: (1) KLB-1 peridotite melting at ambient mantle T_P (1315°C; McKenzie *et al.*, 2005); (2) KG1(8) pyroxenite melting at ambient T_P; (3) KLB-1 peridotite melting at $T_P = 1500^\circ$C; (4) KG1(8) pyroxenite melting at $T_P = 1500^\circ$C.

To model decompression melting, an equilibrium isentropic *P*–*T* path was calculated using the method of Katz *et al.* (2003). Melt productivity as a function of pressure, dF/dP, is calculated according to the set of equations given by Katz *et al.* (2003), where melting is split into a high-productivity clinopyroxene-bearing region and a subsequent lower productivity clinopyroxene-absent region. These two melting regimes can be seen in all lithologies in Fig. 9, in addition to the quartz-bearing interval in N-MORB. *P*–*T*–*F* path calculations are performed separately for a mantle of KLB-1 peridotite and the $X = 0{\cdot}5$ KG1(8) pyroxenite compositions; that is, heat flow between the two lithologies in a mixed source mantle is not considered (see Phipps Morgan, 2001). A detailed description of the method and new parameterization for pyroxenite melting are given in the Appendix.

T and P were calculated at $F = 0{\cdot}01$ steps from the intersection of the relevant adiabat with the corresponding solidus; this structure was used as a basis for melt composition calculations. The *P*–*T*–*F* structure is calculated using a simplified assumption of thermal equilibrium between a single lithology and its partial melt. However, its effectiveness as an approximation for use in accumulated incremental batch melting simulations can be confirmed by comparing the input temperature and the model (THERMOCALC output) temperature at a given pressure and melt fraction. The results show that the input and output temperatures generally match well, with a maximum difference at a given P and F of 42°C before clinopyroxene is exhausted from the residue (Fig. 11). This means that the imposed equilibrium thermal structure is close to the model fractional melting thermal structure until clinopyroxene exhaustion, and is an adequate way of imposing a dynamic melting regime in THERMOCALC. The output *P*–*T* path tracks the shift in the solidus to higher temperatures as the bulk composition depletes, and inflections in the output *P*–*T* path, seen in Fig. 11, reflect changes in residual mineral composition (usually the loss of a phase). Once clinopyroxene is lost from the KLB-1 residue at $F \sim 0{\cdot}2$, the temperature required to produce a further 1% melt increases momentarily with a decrease in pressure. This pause in melting is expected, given that in fractional melting the solidus temperature will increase when a phase is lost [similar to the findings of Asimow *et al.* (1995)]. Beyond this point, momentary temperature increases were dealt with by skipping melting steps (see Appendix). The melting path for KG1(8) is much longer because clinopyroxene remains in the residue until $F \sim 0{\cdot}6$.

Melt composition

Fractional melts are thought to accumulate and mix at the base of the crust, and primitive magmas are generally well-mixed averages of fractional melts (Kelemen *et al.*, 1997; Jennings *et al.*, 2017), although examples of incomplete mixing are also found in melt inclusions and within whole-rock samples from single volcanic systems or lava flows (e.g. Sobolev & Shimizu, 1994; Maclennan *et al.*, 2003). The incremental melt compositions retrieved along the polybaric fractional melting paths (described above) are integrated to simulate this process of recombination. For simplicity, the integration is performed here using a 1D melting column geometry without compaction, such that a given accumulated melt fraction is the average of the cumulative melt

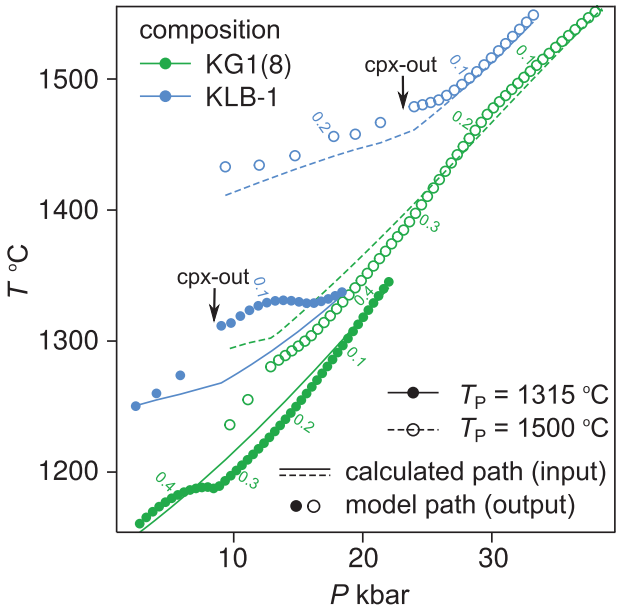

Fig. 11. Calculated [input, calculated by method of Katz *et al.* (2003)] and model (output, temperature results from THERMOCALC) for fractional melting model. Blue, KLB-1; green, KG1(8); continuous line, $T_P = 1315°C$ input *P*–*T* path; dashed line, $T_P = 1500°C$ input *P*–*T* path; filled points, output *P*–*T* path at $T_P = 1315°C$; open points, output *P*–*T* path at $T_P = 1500°C$. All points in $F = 0{\cdot}01$ steps; small numbers show $F = 0{\cdot}1$ intervals.

fractions (e.g. a melt given as $F = 0{\cdot}03$ is the average of the first three incremental melts, where the calculation is performed in steps of $F = 0{\cdot}01$).

The evolution of these incremental and accumulated fractional melts with further decompression, thus increasing cumulative *F*, is shown in terms of five oxides in Fig. 12. T_P is a proxy for average depth of melting, as hotter decompressing mantle will intersect the solidus and begin to melt at higher pressure and temperature. As was also indicated by Fig. 10, Fig. 12 shows that the melt composition is a function of both source composition and depth of melting, making it more difficult to interpret source lithology from the major element composition of erupted magmas. In general, deeper (higher pressure) accumulated fractional melts are lower in Al_2O_3 and higher in CaO (at low melt fractions), MgO and FeO for a given composition. Melts from pyroxenite are higher in FeO and lower in CaO, MgO and Al_2O_3 than melts from peridotite at a given T_P. The fraction of melting reached has some importance; for example, high-fraction pyroxenite melts ($F > 0{\cdot}4$) have a similar composition to low-fraction peridotite melts in terms of FeO and CaO. Interestingly, shallower peridotite partial melts from ambient temperature melting become more enriched in MgO with increased melting and source depletion, whereas deeper peridotite and all pyroxenite melts decrease in MgO with continued melting. This reflects the competing effects of source composition (which would produce more MgO-rich melts with depletion) and depth (which would produce less MgO-rich melts as pressure decreases) on the melt.

The Fo contents of olivine in the solid mantle residue are also shown in Fig. 12c. This shows Fo to increase with increasing extent of melt extraction. KG1(8) pyroxenite mantle olivine ranges from 82·8 to 89·5 and varies predominantly as a function of melt fraction. Primary pyroxenite-derived melts are therefore not required to be in equilibrium with high-Fo (>90) olivine, provided that the melts maintain Fe–Mg disequilibrium with peridotite.

In summary, the Al_2O_3 and MgO of mantle melts appear to be more sensitive to pressure than to source composition, whereas CaO and FeO are more sensitive to source composition than to pressure. CaO and FeO may therefore be the more useful indicators of source lithology, although their concentrations are still affected by the depth of melting. This is consistent with the identification of an enriched end-member for magmas on Iceland, which is characterized by high FeO and low CaO as well as enriched trace elements, representing melting of a fusible component in the mantle (Shorttle and Maclennan, 2011).

Application to the origin of high-Fe mantle melts (ferropicrites)

Although thermodynamic and empirical models based on melting of peridotite can explain the nature of melting regimes involved in the generation of the parental melts of picrites and olivine basalts (e.g. Langmuir *et al.*, 1992; Ghiorso *et al.*, 2002; Herzberg & O'Hara, 2002; Herzberg & Asimow, 2008, 2015), these models do not account for the genesis of primitive mantle melts that are anomalously rich in Fe (e.g. $FeO_T \geq MgO$). These so-called ferropicrites are subalkaline with > 12 wt % MgO and have noticeably lower Al_2O_3 and CaO contents (both <approximately 10 wt %) than mantle-derived picrites (Gibson, 2002). Ferropicrites were first identified in the Western Superior Province Archaean greenstone belt (Hanski & Smolkin, 1989) and have since been identified throughout the geological record. Examples of Phanerozoic ferropicrites are rare, and are found exclusively in large igneous province settings: in CFB provinces including Emeishan, Siberian Traps, Karoo, Paraná–Etendeka, Madagascar, North Atlantic and Ethiopian CFB provinces (Lightfoot *et al.*, 1990; Wooden *et al.*, 1993; Fram & Lesher, 1997; Storey *et al.*, 1997; Ewart *et al.*, 1998; Gibson *et al.*, 2000; Gibson, 2002; Riley *et al.*, 2005; Zhang *et al.*, 2006; Heinonen & Luttinen, 2008; Heinonen *et al.*, 2010; Desta *et al.*, 2014), and in possible accreted oceanic plateaus (Ichiyama *et al.*, 2006; Erdenesaikhan *et al.*, 2014).

The most common hypothesis adopted to explain the origin of Phanerozoic ferropicrites is that they represent near-primary partial melts of pyroxenite, which formed at high *P* and *T* in the convecting mantle. This model was first suggested by Gibson (2002), who noted that the hybrid pyroxenite produced in the peridotite–eclogite sandwich experiments of Yaxley &

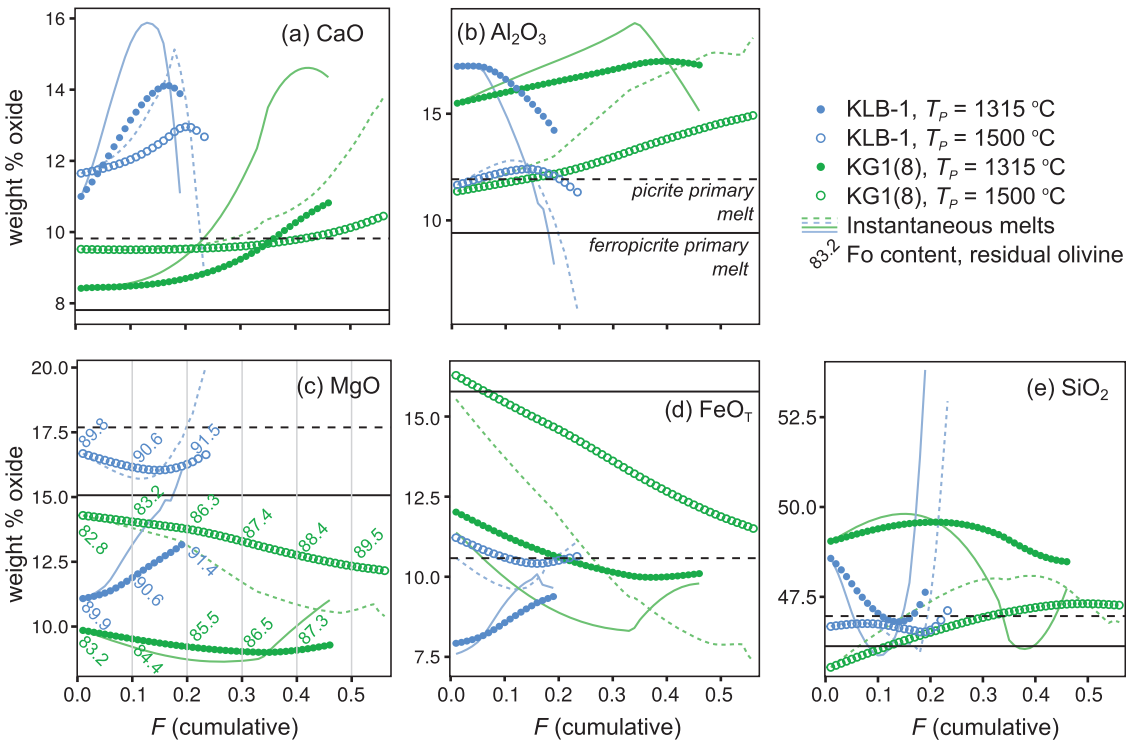

Fig. 12. Composition of accumulated fractional melts as a function of melt fraction *F*. (a) CaO, (b) Al_2O_3, (c) MgO, (d) FeO_T and (e) SiO_2, for polybaric fractional melting of peridotite KLB-1 (blue) and silica-deficient pyroxenite KG1(8) (green) and $T_P = 1315$ and 1500°C. Each point represents an $F = 0{\cdot}01$ calculation step. Points show the integrated cumulative melt compositions of all melt fractions up to the one given. Lines show the instantaneous melt compositions. A 1D melt column is assumed; that is, the composition of an $F = 0{\cdot}03$ melt is the average of the $F = 0{\cdot}01$, 0·02 and 0·03 incremental melt compositions. Lines show the Paraná–Etendeka CFB province picrite (continuous line) and ferropicrite (dashed line) suggested primary melt compositions for comparison, calculated assuming $Fe^{3+}/Fe_T = 0{\cdot}1$. Plot (c) also shows the Fo content [100(Mg/(Mg + Fe^{2+})), mol] of olivine in the solid mantle residue at melting intervals of 0.1, where the colour indicates the corresponding bulk composition.

Green (1998) was enriched in FeO_T. Tuff *et al.* (2005) subsequently strengthened this hypothesis by examining the high-pressure phase relations of a ferropicrite from the Paraná–Etendeka CFB province. In their experiments, they found that garnet and clinopyroxene were co-saturated at pressures above 3 GPa, indicating equilibrium with a high-pressure garnet- and clinopyroxene-bearing source. Such a hypothesis is consistent with the observation that ferropicrites represent early magmatism in CFB provinces: the thick lithosphere prior to extensive rifting would restrict partial melting in an upwelling mantle plume to only more fusible lithologies (Gibson, 2002). This model is consistent with Sr, Nd, Pb and Os isotopic and trace element compositions of ferropicrites from the Karoo CFB province (Heinonen *et al.*, 2013, 2014). The source pyroxenite has been suggested to be Fe-enriched, to explain the high Fe content of ferropicrites (Ichiyama *et al.*, 2006).

Alternative mechanisms of ferropicrite genesis have also been proposed. It has been suggested that ferropicrite melts derive from mixing of immiscible Fe-rich melts with picrites (Jakobsen *et al.*, 2005; Veksler *et al.*, 2006), although Goldstein & Francis (2008) noted that ferropicrite crystallization temperatures and MgO contents are too high to be consistent with this model. Archaean ferropicrites are frequently suggested to have formed by partial melting of an Fe-rich peridotitic mantle source (in the sense that the Mg# is decreased by FeO addition rather than MgO reduction), although the origin of this Fe enrichment is uncertain: an initially Fe-rich mantle and subsequent Fe sequestration, a core contribution, and even an infall of Fe-rich chondritic meteorites have been suggested (Hanski & Smolkin, 1995; Stone *et al.*, 1995; Francis *et al.*, 1999; Gibson *et al.*, 2000; Goldstein & Francis, 2008; Milidragovic & Francis, 2015).

The final part of this study uses a thermodynamic approach to investigate whether the major element compositions of ferropicrites are indeed compatible with melting of pyroxenite. If the pyroxenite hypothesis is correct, then the presence of ferropicrites in several CFB provinces implies the presence of pyroxenite, or originally eclogite, in the CFB mantle sources. If these mantle sources are in fact mantle plume starting heads that originated at the core–mantle boundary (Richards *et al.*, 1989; Campbell & Griffiths, 1990), then the presence of eclogite has important implications for the deep cycling of older subducted slabs into regions of plume initiation. The pyroxenite hypothesis negates the requirement for anomalously Fe-rich mantle peridotite domains to exist, along with the array of processes suggested to produce them.

Major element composition of accumulated pyroxenite partial melts

The unusual major element chemistry of ferropicrites is one of their most conspicuous features. Yet, because major element modelling requires thermodynamic analysis (and an appropriate thermodynamic tool for pyroxenite melting was not previously available), its investigation has thus far been restricted to (1) comparison with experimental melt compositions (e.g. Gibson, 2002; Goldstein & Francis, 2008), (2) comparison with published major element markers of pyroxenite partial melts (Heinonen *et al.*, 2013), and (3) experimental examination of their high-pressure liquidus phase relationships (Tuff *et al.*, 2005). In this section, the compositions of primitive ferropicrites from the Paraná–Etendeka CFB province are compared with modelled accumulated fractional melts to investigate whether pyroxenite partial melting at high pressure is indeed responsible for their origin. For comparison, picrites and basalts from the same province ('Horingbaai-type picrites'; Thompson *et al.*, 2001) are also examined. These are thought to be derived from high-temperature decompression melting of peridotitic mantle (Thompson *et al.*, 2001).

The compositions of primary melts (normalized to 100% in the eight-component NCFMASCrO system and shown in Figs 12 and 13) were calculated as follows. For the picrites, the whole-rock sample with the highest Fo olivine [sample 97SB33 with $Fo_{85–93}$ olivine of Thompson *et al.* (2001)] was adjusted to be in $K_D^{Fe–Mg}$ equilibrium with the average sample Fo (91·6) by adding equilibrium olivine (assuming a melt $Fe^{3+}/\Sigma Fe = 0{\cdot}1$) using PRIMELT3 (Herzberg & Asimow, 2015), corresponding to a primary composition of 17·7 wt % MgO. For comparison, the maximum Fo olivines (93·3) are in equilibrium with a 21·6 wt % MgO liquid. For the ferropicrites, the most primitive and unaltered sample was chosen [sample 97SB63 with up to Fo_{86} olivine, from Gibson *et al.* (2000)]. Its composition was corrected to be in equilibrium with the highest Fo olivine (86·0), at MgO = 15·1 wt % (also with melt $Fe^{3+}/\Sigma Fe = 0{\cdot}1$), which assumes that there had been no significant prior fractionation and that these olivines are in equilibrium with their mantle source. On the solidus of KG1(8) at $T_P = 1500°C$, olivine is $Fo_{82·9}$ in the present model, which steadily increases during decompression fractional melting (Fig. 12). Therefore, $Fo_{86·0}$ or lower does not necessarily imply prior olivine fractionation in pyroxenite-derived melts.

Figure 12 shows the suggested primary melt composition of Etendeka picrites and ferropicrites. FeO_T (ΣFe as FeO), rather than FeO, is shown in Fig. 12, to reduce the effect of (1) choice of $Fe^{3+}/\Sigma Fe$ in the mantle source and (2) assignment of $Fe^{3+}/\Sigma Fe$ in the natural samples on the comparability of the two. The picrites and ferropicrites do not perfectly coincide with any given source composition, T_P, or F, reflecting both the large uncertainty associated with determining a primary composition and the simplified nature of the model. However, for every oxide shown, the general sense of the difference between the picrite and ferropicrite primary melt is consistent with the derivation of ferropicrite from a source more similar to KG1 pyroxenite, whereas picrite is more consistent with a peridotite source (i.e. ferropicrite is higher in FeO_T and lower in CaO, Al_2O_3 and MgO), and is generally consistent with a high T_P in the region of ~1500°C.

The composition of accumulated fractional melts plotted in terms of the co-variation of two compositional parameters is shown in Fig. 13. Figure 13a is a plot of melt CaO versus MgO; this combination of oxides was suggested by Herzberg & Asimow (2008) to be useful in discriminating between peridotite and pyroxenite sources. It does indeed appear to provide good discrimination between melts of the two sources from this study. The grey dashed line was used by Herzberg & Asimow (2008) as a practical way to identify peridotite-sourced melts (which plot above the line) and pyroxenite-sourced melts (which plot below it) in the software PRIMELT2 and 3 (Herzberg & Asimow, 2008, 2015). Fractionation of olivine will shift melt compositions parallel to the peridotite–pyroxenite divide, so will not cause liquids to cross it. The divide was suggested on the basis of a parameterization of melting experiments, although Herzberg (2011) noted that it is not necessarily applicable in all circumstances. Although KG1(8)-derived melts do indeed plot beneath it, it is difficult to discriminate between high-fraction pyroxenite melts and low-fraction, low-pressure peridotite melts. Melting of pyroxenite at $T_P > 1500°C$ would probably produce melts that cross the proposed dividing line. In addition, the compositional change from peridotites through to pyroxenites is not a sharp boundary, and partial melts from an intermediate composition would plot closer to the divide. This discriminatory boundary is useful, however, because it is insensitive to olivine fractionation and different primary compositions related to erupted magmas along an olivine-only control line can be distinguished.

As discussed above, the CaO and FeO_T contents of melts are somewhat more sensitive to source composition than to depth of melting, and the reverse is true for MgO and Al_2O_3. If CaO and FeO_T concentrations are normalized to the more pressure-sensitive MgO or Al_2O_3, then the depth effect is reduced (as is done in Fig. 13b and c). As a result, more of the variation in the plotted melt compositions and natural samples is accounted for by changes in the source composition. Figure 13b is normalized to Al_2O_3, which means that olivine fractionation will have a minor effect on the melt composition in this plot, so the accurate estimation of a primary melt is less critical in discriminating between a peridotite source (which is indicated by melts with low FeO_T/Al_2O_3 and high CaO/Al_2O_3) and a pyroxenite source. In Fig. 13c, the effect of olivine fractionation is pronounced; despite this, a separation of peridotite- and pyroxenite-sourced melts is still achieved, with

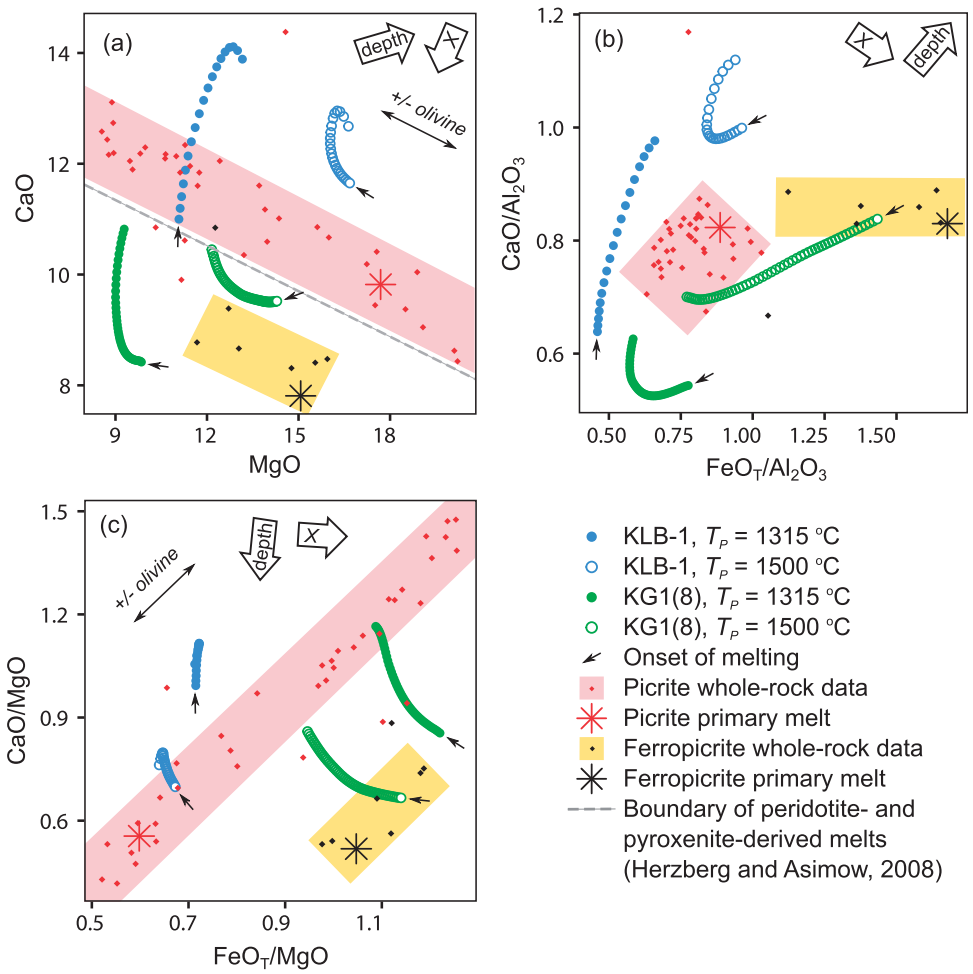

Fig. 13. Composition of accumulated fractional melts compared with whole-rock data. Points are accumulated (integrated) melt compositions at $F = 0{\cdot}01$ intervals (see caption to Fig. 12 for details). Small arrows indicate the location of the $F = 0{\cdot}01$ melt (i.e. the onset of melting). Small dots represent unfiltered whole-rock samples from the Etendeka province [normalized to 100% in the eight-component NCFMASCrO system; data from Gibson *et al.* (2000) and Thompson *et al.* (2001)], enclosed by coloured fields to highlight the general trend and location of most of the samples, and stars show the suggested primary melt compositions. Vectors calculated for olivine fractionation/accumulation are shown, and explain most of the spread in the whole-rock data. Short white arrows show the approximate effects of increasing depth of melting and source enrichment (*X*) on the liquid composition. The dashed line in (a) is the boundary given by Herzberg & Asimow (2008) to differentiate between peridotite-derived melts (above the line) and pyroxenite-derived melts (below the line), where change parallel to the line is caused by olivine loss or gain.

only small differences in melt composition resulting from varying T_P.

It is concluded that CaO and $FeO_{(T)}$ in a magma are the best major elements for discriminating between source compositions, and that these can be normalized to either MgO or Al_2O_3 to reduce the complicating effect of pressure on magma composition. This is in agreement with previous studies. For example, isotopically enriched samples from Iceland have higher FeO_T and lower CaO and SiO_2 than isotopically depleted samples and have been shown to be derived from more fusible mantle lithologies (Shorttle & Maclennan, 2011; Sims *et al.*, 2013). Additionally, Lambart *et al.* (2013) showed from experimental data that pyroxenite-derived melts can have high FeO and/or low SiO_2 relative to peridotite-derived melts. In the modelled fractional accumulated melts of this study, SiO_2 is similar for KG1(8) pyroxenite and KLB-1 peridotite, although it is lower at higher pressure. Some features of the major element geochemistry of OIB that are incompatible with a peridotite source (e.g. at the same SiO_2 content, they tend to be higher in FeO_T and lower in CaO than 3 GPa near-solidus peridotite partial melts) could also be reconciled if a proportion of silica-undersaturated pyroxenite were present in their mantle source (e.g. Kogiso *et al.*, 1998; Davis *et al.*, 2011).

Paraná–Etendeka picrite and ferropicrite whole-rock compositions and suggested primary melt compositions are also shown in Fig. 13. It is clearer here than in Fig. 12 that (1) ferropicrites are similar to low- to moderate-fraction melts of high-pressure (high-T_P) silica-deficient pyroxenite KG1 and (2) picrites are similar to partial melts of KLB-1 peridotite. The dominating effect of olivine loss or gain on the whole-rock compositions is clear in Fig. 13a and c. In every plot, the sense of the change in chemistry between picrites and

ferropicrites is matched by the sense of change between accumulated fractional melts of KLB-1 and KG1(8). The chemistries of the natural samples could probably be better matched by calculating over a wider range of T_P and adjusting the bulk composition, although the examples shown clearly illustrate that ferropicrites can be explained by high-pressure melting of a predominantly pyroxenitic source. There is little consensus about the most appropriate composition for mantle pyroxenite, and KG1 by no means represents the only option: being a synthetic mixture of MORB and peridotite, it is not entirely clear how such a blended composition would be created in the mantle.

Implications for whole-mantle recycling. It is concluded major-element chemistry of picrites and ferropicrites from the Paraná–Etendeka CFB province can be accounted for by elevated-temperature melting of peridotite and pyroxenite, respectively, in agreement with previous studies (Thompson *et al.*, 2001; Gibson, 2002; Tuff *et al.*, 2005). If ferropicrites are the result of partial melting of pyroxenite at elevated temperatures, then their presence in several Phanerozoic CFB provinces implies that CFB mantle sources are generally lithologically heterogeneous. To produce a pyroxenitic lithology, a two-step model involving the initial partial melting of eclogite and subsequent metasomatism of peridotite is a possibility. The presence of ferropicrites in CFB settings therefore implies that recycled eclogitic material is present in CFB mantle sources. If mantle plume starting heads are responsible for CFB provinces (Richards *et al.*, 1989; Campbell & Griffiths, 1990), and if these derive from the core–mantle boundary, then this implies that subducted slab material has undergone whole-mantle cycling and has been advected to the surface from regions of plume nucleation (e.g. Hofmann, 1997), or recycled material may have been entrained by the plume head at storage interfaces in the mid-mantle. However, ferropicrite outcrops are volumetrically minor and do not constrain the proportion of eclogite or pyroxenite in CFB mantle sources.

Limitations

The thermodynamic model of Jennings & Holland (2015) is tested in this study for applicability to a range of potential mantle compositions. It should be used with caution, especially for assemblages containing a free silica phase, and the effect of several model limitations must be considered. The solid–liquid Fe–Mg partitioning behaviour of the model becomes unreliable at pressures above around 50 kbar (Jennings & Holland, 2015), which may be relevant to the genesis of ferropicrites (although it is noted that Figs 2 and 4 show that experimental melt Mg and Fe contents are effectively reproduced at 30 kbar in pyroxenite and eclogite).

Perhaps a more serious limitation when examining the melting behaviour of enriched mantle compositions is that calculations are performed in the simple NCFMASOCr system. This is used to approximate a real, complex system, and is appropriate for calculating peridotite phase relations. However, TiO_2, K_2O, H_2O and CO_2 are not examined; these components will affect the phase equilibria, liquid composition, melt productivity and, most significantly, the solidus temperature (Green, 1973; Eggler, 1976; Gaetani & Grove, 1998; Dasgupta & Hirschmann, 2007; Davis & Hirschmann, 2013). This becomes a more important limitation when considering pyroxenite and eclogite, which contain higher concentrations of all of these elements than peridotite. Some experimental studies on eclogite melting have stabilized rutile and K-feldspar close to the solidus, although these phases are lost shortly after the onset of melting (Spandler *et al.*, 2008). Because TiO_2, K_2O and H_2O are higher in ferropicrites than in picrites [e.g. up to 4% TiO_2 in samples from the Karoo (Riley *et al.*, 2005)], the system limitation is particularly important when using the present model to investigate their origin. In detail, including these elements will have some effect on the melt concentrations of the components considered in this study, in particular by moving low-fraction melting to higher pressures. Overall, however, this system limitation should not affect the conclusion that ferropicrites have more major element compositional similarities to partial melts of mantle pyroxenite than to peridotite. The anticipated lowering of the pyroxenite solidus by the neglected components may actually promote the production of more ferropicritic partial melts.

CONCLUSIONS

In this study, the thermodynamic model of Jennings & Holland (2015) was tested to validate its use in investigating the relationship between primary melts and mantle composition. Despite being calibrated for peridotite melting, it was found that the model could effectively reproduce experimental partial melt compositions for the pyroxenite KG1 (Kogiso *et al.*, 1998) and eclogite G2 (Pertermann & Hirschmann, 2003*a*); the latter contains a free silica phase at pressures above 18·3 kbar, indicating the activation of the garnet–pyroxene thermal divide.

The thermodynamic model was used to investigate the relationship between source composition and melting behaviour. The thermal divide was found to have a dominant control on solidus temperature, melt productivity, and partial melt composition. When considering only olivine-bearing lithologies (i.e. silica-deficient bulk compositions at all pressures and more silica-rich compositions at low pressures), the dependence of melt temperature and composition on bulk composition was found to be strongly non-linear. The concentrations of most oxides in partial melts from more enriched bulk compositions tend to be buffered by the increased stability of more fusible phases (in particular clinopyroxene). This means that partial melts of pyroxenite are not very different from those of peridotite, as previously noted by Lambart *et al.* (2013), despite the difference in

mineral modes and bulk composition. An exception to this is in FeO, where the concentration in the melt has a strong response to the changing bulk composition, despite the fact that the range of FeO is small across the bulk compositions considered. This is the result of the $K_D^{Fe–Mg}$ control on the melt composition and the lower bulk MgO in the more enriched compositions. Some melt oxide concentrations, in particular Al_2O_3 and MgO, were found to be more sensitive to pressure than to bulk composition. The solidus temperature is fairly insensitive to bulk composition, although from the onset of melting, more enriched bulk compositions melt more productively over a greater melt fraction interval.

The changes in melt composition in response to bulk composition were exploited to examine the hypothesis that high-Fe mantle melts are derived from partial melting of mantle pyroxenite. The results of our modelling show that the conspicuously high FeO_T in ferropicrites does not require a high-Fe mantle source with peridotitic MgO contents and is indeed best explained by low to moderate fraction pyroxenite melting, as is their low CaO content. The low Al_2O_3 characteristic of ferropicrites reflects their relatively high pressure of formation and supports a model involving melting of pyroxenite in hot mantle plume starting heads, restricted to high pressures and low fractions beneath thick lithosphere (Gibson, 2002).

In this study, ferropicrite compositions are compared with modelled accumulated fractional melts of the hypothetical pyroxenite KG1 (Kogiso *et al.*, 1998). This composition is merely illustrative of the types of melt compositions expected from a more enriched mantle and is not suggested to be the best match for the ferropicrite source. The range of pyroxenite and eclogite compositions that have been considered in experimental studies, and those that may actually exist in the mantle, is huge (e.g. Lambart *et al.*, 2013), and heterogeneity may be introduced into the mantle by a variety of mechanisms (e.g. Herzberg, 2011). A thermodynamic approach such as the one used here can be used to further investigate the origin and consequences of mantle heterogeneity.

FUNDING

This work was supported by a Natural Environment Research Council studentship (NE/J500070/1) to E.S.J. and Natural Environment Research Council grant (NE/J021539/1) to J.M. and T.J.B.H.

SUPPLEMENTARY DATA

Supplementary data for this paper are available at *Journal of Petrology* online.

ACKNOWLEDGEMENTS

We thank Claude Herzberg, Tetsu Kogiso and Fred Davis for their thoughtful and thorough reviews, which improved the scientific discussion and presentation of this study. In addition, we thank Marjorie Wilson for comments and editorial handling.

REFERENCES

Asimow, P. D., Hirschmann, M. M., Ghiorso, M. S., O'Hara, M. J. & Stolper, E. M. (1995). The effect of pressure-induced solid–solid phase transitions on decompression melting of the mantle. *Geochimica et Cosmochimica Acta* **59**, 4489–4506.

Blundy, J. D., Falloon, T. J., Wood, B. J. & Dalton, J. A. (1995). Sodium partitioning between clinopyroxene and silicate melts. *Journal of Geophysical Research: Solid Earth* **100**, 15501–15515.

Campbell, I. H. & Griffiths, R. W. (1990). Implications of mantle plume structure for the evolution of flood basalts. *Earth and Planetary Science Letters* **99**, 79–93.

Canil, D., O'Neill, H. S. C., Pearson, D. G., Rudnick, R. L., McDonough, W. F. & Carswell, D. A. (1994). Ferric iron in peridotites and mantle oxidation states. *Earth and Planetary Science Letters* **123**, 205–220.

Chauvel, C., Hofmann, A. W. & Vidal, P. (1992). HIMU–EM: the French Polynesian connection. *Earth and Planetary Science Letters* **110**, 99–119.

Cottrell, E. & Kelley, K. A. (2011). The oxidation state of Fe in MORB glasses and the oxygen fugacity of the upper mantle. *Earth and Planetary Science Letters* **305**, 270–282.

Dasgupta, R. & Hirschmann, M. M. (2007). Effect of variable carbonate concentration on the solidus of mantle peridotite. *American Mineralogist* **92**, 370–379.

Dasgupta, R., Jackson, M. G. & Lee, C.-T. A. (2010). Major element chemistry of ocean island basalts—Conditions of mantle melting and heterogeneity of mantle source. *Earth and Planetary Science Letters* **289**, 377–392.

Davis, F. A. & Hirschmann, M. M. (2013). The effects of K_2O on the compositions of near-solidus melts of garnet peridotite at 3 GPa and the origin of basalts from enriched mantle. *Contributions to Mineralogy and Petrology* **166**, 1029–1046.

Davis, F. A., Tangeman, J. A., Tenner, T. J. & Hirschmann, M. M. (2009). The composition of KLB-1 peridotite. *American Mineralogist* **94**, 176–180.

Davis, F. A., Hirschmann, M. M. & Humayun, M. (2011). The composition of the incipient partial melt of garnet peridotite at 3 GPa and the origin of OIB. *Earth and Planetary Science Letters* **308**, 380–390.

Desta, M. T., Ayalew, D., Ishiwatari, A., Arai, S. & Tamura, A. (2014). Ferropicrite from the Lalibela area in the Ethiopian large igneous province. *Journal of Mineralogical and Petrological Sciences* **109**, 191–207.

Dupré, B. & Allègre, C. J. (1983). Pb–Sr isotope variation in Indian Ocean basalts and mixing phenomena. *Nature* **303**, 142–146.

Eggler, D. H. (1976). Does CO_2 cause partial melting in the low-velocity layer of the mantle? *Geology* **4**, 69–72.

Erdenesaikhan, G., Ishiwatari, A., Orolmaa, D., Arai, S. & Tamura, A. (2014). Discovery of ferropicrites and high-magnesian andesites from the Erdenetsogt Formation, Central Mongolia. *Proceedings of the Mongolian Academy of Sciences* **54**, 52–63.

Ewart, A., Milner, S. C., Armstrong, R. A. & Dungan, A. R. (1998). Etendeka volcanism of the Goboboseb Mountains and Messum Igneous Complex, Namibia. Part I: Geochemical evidence of early Cretaceous Tristan plume melts and the role of crustal contamination in the Paraná–Etendeka CFB. *Journal of Petrology* **39**, 191–225.

Falloon, D. T. J. & Green, D. H. (1987). Anhydrous partial melting of MORB pyrolite and other peridotite compositions at 10 kbar: Implications for the origin of primitive MORB glasses. *Mineralogy and Petrology* **37**, 181–219.

Fram, M. S. & Lesher, C. E. (1997). Generation and polybaric differentiation of East Greenland early Tertiary flood basalts. *Journal of Petrology* **38**, 231–275.

Francis, D., Ludden, J., Johnstone, R. & Davis, W. (1999). Picrite evidence for more Fe in Archean mantle reservoirs. *Earth and Planetary Science Letters* **167**, 197–213.

Gaetani, G. A. & Grove, T. L. (1998). The influence of water on melting of mantle peridotite. *Contributions to Mineralogy and Petrology* **131**, 323–346.

Gale, A., Dalton, C. A., Langmuir, C. H., Su, Y. & Schilling, J.-G. (2013). The mean composition of ocean ridge basalts. *Geochemistry, Geophysics, Geosystems* **14**, 489–518.

Ghiorso, M. S. & Sack, R. O. (1995). Chemical mass transfer in magmatic processes IV. A revised and internally consistent thermodynamic model for the interpolation and extrapolation of liquid–solid equilibria in magmatic systems at elevated temperatures and pressures. *Contributions to Mineralogy and Petrology* **119**, 197–212.

Ghiorso, M. S., Hirschmann, M. M., Reiners, P. W. & Kress, V. C. (2002). The pMELTS: A revision of MELTS for improved calculation of phase relations and major element partitioning related to partial melting of the mantle to 3 GPa. *Geochemistry, Geophysics, Geosystems* **3**, 1–35.

Gibson, S. A. (2002). Major element heterogeneity in Archean to Recent mantle plume starting-heads. *Earth and Planetary Science Letters* **195**, 59–74.

Gibson, S. A., Thompson, R. N. & Dickin, A. P. (2000). Ferropicrites: geochemical evidence for Fe-rich streaks in upwelling mantle plumes. *Earth and Planetary Science Letters* **174**, 355–374.

Gibson, S. A., Thompson, R. N., Day, J. A., Humphris, S. E. & Dickin, A. P. (2005). Melt-generation processes associated with the Tristan mantle plume: Constraints on the origin of EM-1. *Earth and Planetary Science Letters* **237**, 744–767.

Goldstein, S. B. & Francis, D. (2008). The petrogenesis and mantle source of Archaean ferropicrites from the Western Superior Province, Ontario, Canada. *Journal of Petrology* **49**, 1729–1753.

Green, D. H. (1973). Experimental melting studies on a model upper mantle composition at high pressure under water-saturated and water-undersaturated conditions. *Earth and Planetary Science Letters* **19**, 37–53.

Green, D. H. & Ringwood, A. E. (1967). An experimental investigation of the gabbro to eclogite transformation and its petrological applications. *Geochimica et Cosmochimica Acta* **31**, 767–833.

Hanski, E. J. & Smolkin, V. F. (1989). Pechenga ferropicrites and other early Proterozoic picrites in the eastern part of the Baltic Shield. *Precambrian Research* **45**, 63–82.

Hanski, E. J. & Smolkin, V. F. (1995). Iron- and LREE-enriched mantle source for early Proterozoic intraplate magmatism as exemplified by the Pechenga ferropicrites, Kola Peninsula, Russia. *Lithos* **34**, 107–125.

Hauri, E. H. (1996). Major-element variability in the Hawaiian mantle plume. *Nature* **382**, 415–419.

Heinonen, J. S. & Luttinen, A. V. (2008). Jurassic dikes of Vestfjella, western Dronning Maud Land, Antarctica: Geochemical tracing of ferropicrite sources. *Lithos* **105**, 347–364.

Heinonen, J. S., Carlson, R. W. & Luttinen, A. V. (2010). Isotopic (Sr, Nd, Pb, and Os) composition of highly magnesian dikes of Vestfjella, western Dronning Maud Land, Antarctica: A key to the origins of the Jurassic Karoo large igneous province?. *Chemical Geology* **277**, 227–244.

Heinonen, J. S., Luttinen, A. V., Riley, T. R. & Michallik, R. M. (2013). Mixed pyroxenite–peridotite sources for mafic and ultramafic dikes from the Antarctic segment of the Karoo continental flood basalt province. *Lithos* **177**, 366–380.

Heinonen, J. S., Carlson, R. W., Riley, T. R., Luttinen, A. V. & Horan, M. F. (2014). Subduction-modified oceanic crust mixed with a depleted mantle reservoir in the sources of the Karoo continental flood basalt province. *Earth and Planetary Science Letters* **394**, 229–241.

Herzberg, C. (2011). Identification of source lithology in the Hawaiian and Canary Islands: Implications for origins. *Journal of Petrology* **52**, 113–146.

Herzberg, C. & Asimow, P. D. (2008). Petrology of some oceanic island basalts: PRIMELT2.XLS software for primary magma calculation. *Geochemistry, Geophysics, Geosystems* **9**, Q09001.

Herzberg, C. & Asimow, P. D. (2015). PRIMELT3 MEGA.XLSM software for primary magma calculation: Peridotite primary magma MgO contents from the liquidus to the solidus. *Geochemistry, Geophysics, Geosystems* **16**, 563–578.

Herzberg, C. & O'Hara, M. J. (2002). Plume-associated ultramafic magmas of Phanerozoic age. *Journal of Petrology* **43**, 1857–1883.

Herzberg, C., Raterron, P. & Zhang, J. (2000). New experimental observations on the anhydrous solidus for peridotite KLB-1. *Geochemistry, Geophysics, Geosystems* **1**, 1051.

Herzberg, C., Asimow, P. D., Arndt, N., Niu, Y., Lesher, C. M., Fitton, J. G., Cheadle, M. J. & Saunders, A. D. (2007). Temperatures in ambient mantle and plumes: Constraints from basalts, picrites, and komatiites. *Geochemistry, Geophysics, Geosystems* **8**, Q02006.

Hirschmann, M. M. (2000). Mantle solidus: Experimental constraints and the effects of peridotite composition. *Geochemistry, Geophysics, Geosystems* **1**, 1042.

Hirschmann, M. M. & Stolper, E. M. (1996). A possible role for garnet pyroxenite in the origin of the 'garnet signature' in MORB. *Contributions to Mineralogy and Petrology* **124**, 185–208.

Hirschmann, M. M., Kogiso, T., Baker, M. B. & Stolper, E. M. (2003). Alkalic magmas generated by partial melting of garnet pyroxenite. *Geology* **31**, 481–484.

Hofmann, A. (1997). Mantle geochemistry: the message from oceanic volcanism. *Nature* **385**, 219–229.

Hofmann, A. W. & White, W. M. (1982). Mantle plumes from ancient oceanic crust. *Earth and Planetary Science Letters* **57**, 421–436.

Holland, T. J. B., Hudson, N. F. C., Powell, R. & Harte, B. (2013). New thermodynamic models and calculated phase equilibria in NCFMAS for basic and ultrabasic compositions through the transition zone into the uppermost lower mantle. *Journal of Petrology* **54**, 1901–1920.

Holland, T. J. B. & Powell, R., (2011). An improved and extended internally consistent thermodynamic dataset for phases of petrological interest, involving a new equation of state for solids. *Journal of Metamorphic Geology* **29**, 333–383.

Ichiyama, Y., Ishiwatari, A., Hirahara, Y. & Shuto, K. (2006). Geochemical and isotopic constraints on the genesis of the Permian ferropicritic rocks from the Mino–Tamba belt, SW Japan. *Lithos* **89**, 47–65.

Jackson, M. G. & Dasgupta, R. (2008). Compositions of HIMU, EM1, and EM2 from global trends between radiogenic isotopes and major elements in ocean island basalts. *Earth and Planetary Science Letters* **276**, 175–186.

Jakobsen, J. K., Veksler, I. V., Tegner, C. & Brooks, C. K. (2005). Immiscible iron- and silica-rich melts in basalt petrogenesis documented in the Skaergaard intrusion. *Geology* **33**, 885–888.

Jennings, E. S. & Holland, T. J. B. (2015). A simple thermodynamic model for melting of peridotite in the system NCFMASOCr. *Journal of Petrology* **56**, 869–892.

Jennings, E. S., Gibson, S. A., Maclennan, J. & Heinonen, J. S. (2017). Deep mixing of mantle melts beneath continental flood basalt provinces: Constraints from olivine-hosted melt inclusions in primitive magmas. *Geochimica et Cosmochimica Acta* **196**, 36–57.

Katz, R. F., Spiegelman, M. & Langmuir, C. H. (2003). A new parameterization of hydrous mantle melting. *Geochemistry, Geophysics, Geosystems* **4**, 1073.

Kawabata, H., Hanyu, T., Chang, Q., Kimura, J.-I., Nichols, A. R. L. & Tatsumi, Y. (2011). The petrology and geochemistry of St. Helena alkali basalts: Evaluation of the oceanic crust-recycling model for HIMU OIB. *Journal of Petrology* **52**, 791–838.

Kelemen, P. B., Hirth, G., Shimizu, N., Spiegelman, M. & Dick, H. J. (1997). A review of melt migration processes in the adiabatically upwelling mantle beneath oceanic spreading ridges. *Philosophical Transactions of the Royal Society of London, Series A* **355**, 283–318.

Kogiso, T. & Hirschmann, M. M. (2006). Partial melting experiments of bimineralic eclogite and the role of recycled mafic oceanic crust in the genesis of ocean island basalts. *Earth and Planetary Science Letters* **249**, 188–199.

Kogiso, T., Hirose, K. & Takahashi, E. (1998). Melting experiments on homogeneous mixtures of peridotite and basalt: application to the genesis of ocean island basalts. *Earth and Planetary Science Letters* **162**, 45–61.

Kogiso, T., Hirschmann, M. M. & Frost, D. J. (2003). High-pressure partial melting of garnet pyroxenite: possible mafic lithologies in the source of ocean island basalts. *Earth and Planetary Science Letters* **216**, 603–617.

Kogiso, T., Hirschmann, M. M. & Reiners, P. W. (2004). Length scales of mantle heterogeneities and their relationship to ocean island basalt geochemistry. *Geochimica et Cosmochimica Acta* **68**, 345–360.

Lambart, S., Laporte, D. & Schiano, P. (2009). An experimental study of pyroxenite partial melts at 1 and 1·5 GPa: Implications for the major-element composition of mid-ocean ridge basalts. *Earth and Planetary Science Letters* **288**, 335–347.

Lambart, S., Laporte, D. & Schiano, P. (2013). Markers of the pyroxenite contribution in the major-element compositions of oceanic basalts: Review of the experimental constraints. *Lithos* **160–161**, 14–36.

Langmuir, C. H., Klein, E. M. & Plank, T. (1992). Petrological systematics of mid-ocean ridge basalts: Constraints on melt generation beneath ocean ridges. In: Morgan, J. P., Blackman, D. K. & Sinton, J. M. (eds) *Mantle Flow and Melt Generation at Mid-Ocean Ridges. American Geophysical Union, Geophysical Monograph* **71**, 183–280.

Lightfoot, P. C., Naldrett, A. J., Gorbachev, N. S., Doherty, W. & Fedorenko, V. A. (1990). Geochemistry of the Siberian Trap of the Noril'sk area, USSR, with implications for the relative contributions of crust and mantle to flood basalt magmatism. *Contributions to Mineralogy and Petrology* **104**, 631–644.

Maclennan, J., McKenzie, D., Hilton, F., Gronvold, K. & Shimizu, N. (2003). Geochemical variability in a single flow from northern Iceland. *Journal of Geophysical Research* **108**, 2007.

Mallik, A. & Dasgupta, R. (2012). Reaction between MORB-eclogite derived melts and fertile peridotite and generation of ocean island basalts. *Earth and Planetary Science Letters* **329–330**, 97–108.

McKenzie, D. (1984). The generation and compaction of partially molten rock. *Journal of Petrology* **25**, 713–765.

McKenzie, D., Jackson, J. & Priestley, K. (2005). Thermal structure of oceanic and continental lithosphere. *Earth and Planetary Science Letters* **233**, 337–349.

Milidragovic, D. & Francis, D. (2015). *Ca.* 2·7 Ga ferropicritic magmatism: A record of Fe-rich heterogeneities during Neoarchean global mantle melting. *Geochimica et Cosmochimica Acta* doi:10.1016/j.gca.2015.09.023.

O'Hara, M. J. (1968). The bearing of phase equilibria studies in synthetic and natural systems on the origin and evolution of basic and ultrabasic rocks. *Earth-Science Reviews* **4**, 69–133.

O'Hara, M. J. & Yoder, H. S. (1967). Formation and fractionation of basic magmas at high pressures. *Scottish Journal of Geology* **3**, 67–117.

Pertermann, M. & Hirschmann, M. M. (2003*a*). Anhydrous partial melting experiments on MORB-like eclogite: Phase relations, phase compositions and mineral–melt partitioning of major elements at 2–3 GPa. *Journal of Petrology* **44**, 2173–2201.

Pertermann, M. & Hirschmann, M. M. (2003*b*). Partial melting experiments on a MORB-like pyroxenite between 2 and 3 GPa: Constraints on the presence of pyroxenite in basalt source regions from solidus location and melting rate. *Journal of Geophysical Research* **108**, 2125.

Phipps Morgan, J. (2001). Thermodynamics of pressure release melting of a veined plum pudding mantle. *Geochemistry, Geophysics, Geosystems* **2**, 2000GC000049.

Pilet, S., Hernandez, J., Sylvester, P. & Poujol, M. (2005). The metasomatic alternative for ocean island basalt chemical heterogeneity. *Earth and Planetary Science Letters* **236**, 148–166.

Powell, R., Holland, T. & Worley, B. (1998). Calculating phase diagrams involving solid solutions via non-linear equations, with examples using THERMOCALC. *Journal of Metamorphic Geology* **16**, 577–588.

Prytulak, J. & Elliott, T. (2007). TiO_2 enrichment in ocean island basalts. *Earth and Planetary Science Letters* **263**, 388–403.

Putirka, K. D., Perfit, M., Ryerson, F. J. & Jackson, M. G. (2007). Ambient and excess mantle temperatures, olivine thermometry, and active vs. passive upwelling. *Chemical Geology* **241**, 177–206.

Richards, M. A., Duncan, R. A. & Courtillot, V. E. (1989). Flood basalts and hot-spot tracks: Plume heads and tails. *Science* **246**, 103–107.

Riley, T. R., Leat, P. T., Curtis, M. L., Millar, I. L., Duncan, R. A. & Fazel, A. (2005). Early–middle Jurassic dolerite dykes from western Dronning Maud Land (Antarctica): Identifying mantle sources in the Karoo Large Igneous Province. *Journal of Petrology* **46**, 1489–1524.

Rosenthal, A., Yaxley, G. M., Green, D. H., Hermann, J., Kovács, I. & Spandler, C. (2014). Continuous eclogite melting and variable refertilisation in upwelling heterogeneous mantle. *Scientific Reports* **4**, 6099.

Shorttle, O. & Maclennan, J. (2011). Compositional trends of Icelandic basalts: Implications for short-length scale lithological heterogeneity in mantle plumes. *Geochemistry, Geophysics, Geosystems* **12**, Q11008.

Shorttle, O., Maclennan, J. & Lambart, S. (2014). Quantifying lithological variability in the mantle. *Earth and Planetary Science Letters* **395**, 24–40.

Sims, K. W. W., Maclennan, J., Blichert-Toft, J., Mervine, E. M., Blusztajn, J. & Grönvold, K. (2013). Short length scale

mantle heterogeneity beneath Iceland probed by glacial modulation of melting. *Earth and Planetary Science Letters* **379**, 146–157.

Sleep, N. H. (1984). Tapping of magmas from ubiquitous mantle heterogeneities: An alternative to mantle plumes?. *Journal of Geophysical Research: Solid Earth* **89**, 10029–10041.

Smith, P. M. & Asimow, P. D. (2005). Adiabat_1ph: A new public front-end to the MELTS, pMELTS, and pHMELTS models. *Geochemistry, Geophysics, Geosystems* **6**, Q02004.

Sobolev, A. V. & Shimizu, N. (1994). The origin of typical NMORB: the evidence from a melt inclusion study. *Mineralogical Magazine* **58**, 862–863.

Sobolev, A. V., Hofmann, A. W., Sobolev, S. V. & Nikogosian, I. K. (2005). An olivine-free mantle source of Hawaiian shield basalts. *Nature* **434**, 590–597.

Spandler, C., Yaxley, G., Green, D. H. & Rosenthal, A. (2008). Phase relations and melting of anhydrous K-bearing eclogite from 1200 to 1600°C and 3 to 5 GPa. *Journal of Petrology* **49**, 771–795.

Stone, W. E., Crocket, J. H., Dickin, A. P. & Fleet, M. E. (1995). Origin of Archean ferropicrites: geochemical constraints from the Boston Creek Flow, Abitibi greenstone belt, Ontario, Canada. *Chemical Geology* **121**, 51–71.

Storey, M., Mahoney, J. J. & Saunders, A. D. (1997). Cretaceous basalts in Madagascar and the transition between plume and continental lithosphere mantle sources. In: Mahoney, J. J. & Coffin, M. F. (eds) *Large Igneous Provinces: Continental, Oceanic, and Planetary Flood Volcanism. American Geophysical Union, Geophysical Monograph* **100**, 95–122.

Stracke, A. (2012). Earth's heterogeneous mantle: A product of convection-driven interaction between crust and mantle. *Chemical Geology* **330–331**, 274–299.

Takahashi, E. & Kushiro, I. (1983). Melting of a dry peridotite at high pressures and basalt magma genesis. *American Mineralogist* **68**, 859–879.

Takahashi, E. & Nakajima, K. (2002). Melting process in the Hawaiian plume: an experimental study. In: Takahashi, E., Lipman, P. W., Garcia, M. O., Naka, J. & Aramaki, S. (eds) *Hawaiian Volcanoes: Deep Underwater Perspectives. American Geophysical Union, Geophysical Monograph* **128**, 403–418.

Takahashi, E., Shimazaki, T., Tsuzaki, Y. & Yoshida, H. (1993). Melting study of a peridotite KLB-1 to 6·5 GPa, and the origin of basaltic magmas. *Philosophical Transactions of the Royal Society of London, Series A* **342**, 105–120.

Takahashi, E., Nakajima, K. & Wright, T. L. (1998). Origin of the Columbia River basalts: melting model of a heterogeneous plume head. *Earth and Planetary Science Letters* **162**, 63–80.

Thompson, R. N., Gibson, S. A., Dickin, A. P. & Smith, P. M. (2001). Early Cretaceous basalt and picrite dykes of the southern Etendeka region, NW Namibia: Windows into the role of the Tristan mantle plume in Paraná–Etendeka magmatism. *Journal of Petrology* **42**, 2049–2081.

Tuff, J., Takahashi, E. & Gibson, S. A. (2005). Experimental constraints on the role of garnet pyroxenite in the genesis of high-Fe mantle plume derived melts. *Journal of Petrology* **46**, 2023–2058.

Veksler, I., Dorfman, A., Danyushevsky, L., Jakobsen, J. & Dingwell, D. (2006). Immiscible silicate liquid partition coefficients: implications for crystal–melt element partitioning and basalt petrogenesis. *Contributions to Mineralogy and Petrology* **152**, 685–702.

Wasylenki, L. E., Baker, M. B., Kent, A. J. R. & Stolper, E. M. (2003). Near-solidus melting of the shallow upper mantle: Partial melting experiments on depleted peridotite. *Journal of Petrology* **44**, 1163–1191.

Weaver, B. L. (1991). Trace element evidence for the origin of ocean-island basalts. *Geology* **19**, 123–126.

Willbold, M. & Stracke, A. (2006). Trace element composition of mantle end-members: Implications for recycling of oceanic and upper and lower continental crust. *Geochemistry, Geophysics, Geosystems* **7**, Q04004.

Wooden, J. L., Czamanske, G. K., Fedorenko, V. A., Arndt, N. T., Chauvel, C., Bouse, R. M., King, B.-S. W., Knight, R. J. & Siems, D. F. (1993). Isotopic and trace-element constraints on mantle and crustal contributions to Siberian continental flood basalts, Noril'sk area, Siberia. *Geochimica et Cosmochimica Acta* **57**, 3677–3704.

Yasuda, A., Fujii, T. & Kurita, K. (1994). Melting phase relations of an anhydrous mid-ocean ridge basalt from 3 to 20 GPa: Implications for the behavior of subducted oceanic crust in the mantle. *Journal of Geophysical Research: Solid Earth* **99**, 9401–9414.

Yaxley, G. M. (2000). Experimental study of the phase and melting relations of homogeneous basalt + peridotite mixtures and implications for the petrogenesis of flood basalts. *Contributions to Mineralogy and Petrology* **139**, 326–338.

Yaxley, G. M. & Green, D. H. (1998). Reactions between eclogite and peridotite: Mantle refertilisation by subduction of oceanic crust. *Schweizerische Mineralogische und Petrographische Mitteilungen* **78**, 243–255.

Yaxley, G. & Sobolev, A. (2007). High-pressure partial melting of gabbro and its role in the Hawaiian magma source. *Contributions to Mineralogy and Petrology* **154**, 371–383.

Yoder, H. S. & Tilley, C. E. (1962). Origin of basalt magmas: an experimental study of natural and synthetic rock systems. *Journal of Petrology* **3**, 342–532.

Zhang, Z., Mahoney, J. J., Mao, J. & Wang, F. (2006). Geochemistry of picritic and associated basalt flows of the western Emeishan Flood Basalt Province, China. *Journal of Petrology* **47**, 1997–2019.

Zindler, A. & Hart, S. (1986). Chemical geodynamics. *Annual Review of Earth and Planetary Sciences* **14**, 493–571.

APPENDIX: THERMAL MODEL FOR MELTING

P–T–F pathways for decompression melting were calculated assuming anhydrous and isentropic conditions according to the method of Katz *et al.* (2003), where melting is split into a clinopyroxene-bearing high-productivity interval and a clinopyroxene-absent low-productivity region. The differential equation provided by Katz *et al.* (2003; originally McKenzie, 1984) for dF/dP is numerically integrated using a fourth-order Runge–Kutta scheme. For peridotite melting, the solidus, liquidus and melt productivity parameterization of Katz *et al.* (2003) were used, along with the thermal properties of Shorttle *et al.* (2014). For pyroxenite melting, a new solidus, liquidus and melt productivity parameterization was created for the KG1(8) composition (see Table 1) from calculations using the Jennings & Holland (2015) melt model. In addition, a clinopyroxene-out boundary was defined as a quadratic function of P (although in this study, only the high-productivity region was required). The parameters used are listed in Table A1.

A note on fractional melt modelling beyond clinopyroxene exhaustion

At cumulative melt fractions above cpx-out, the input model overestimates the melt productivity (as seen in subsequent calculated temperature increases); this occurs because the input model is calibrated for equilibrium melting of KLB-1. By $F \sim 0{\cdot}2$, the residual solid from fractional melting is too depleted and will have to decompress further than predicted by the model to produce an additional 1% of melt. To extend calculations to higher cumulative F, we skip decompression steps where a temperature increase is required for equilibrium with 1% melt, allowing the solid to decompress an extra increment before a 1% melt fraction is achieved. The effect of this workaround on the chemistry is minimal.

Table A1: Parameters used in calculating P–T–F path

	KLB-1 peridotite	KG1-a pyroxenite	Unit	Notation
$T_{solidus}$	$993{\cdot}7 + 206{\cdot}4P - 12{\cdot}4P^2$	$941{\cdot}1 + 208{\cdot}9P - 12{\cdot}8P^2$	°C	
$T_{lhz-liq}$	$1901{\cdot}8 - 154{\cdot}6P + 25{\cdot}2P^2$	$1293{\cdot}7 + 67{\cdot}7P + 5{\cdot}3P^2$	°C	
$T_{liquidus}$	$1769{\cdot}2 + 59{\cdot}6P - 3{\cdot}7P^2$	$1507{\cdot}8 + 64{\cdot}2P$	°C	
$T_{cpx-out}$	$1149{\cdot}0 + 144{\cdot}8P - 5{\cdot}3P^2$	$1115{\cdot}5 + 152{\cdot}2P - 6{\cdot}4P^2$	°C	
β_1	1·0	1·0		Melting function exponent, cpx-bearing
β_2	1·5	1·5		Melting function exponent, cpx-absent
c_p	1187*	1140*	J kg^{-1} K^{-1}	Heat capacity (constant pressure)
α_{solid}	$3{\cdot}2 \times 10^{-5}$	$3{\cdot}2 \times 10^{-5}$	K^{-1}	Thermal expansivity, solid
ρ_{solid}	3300*	3300*	kg m^{-3}	Density, solid
ρ_{liq}	2900*	2900*	kg m^{-3}	Density, liquid
ΔS	407*	380*	J kg^{-1} K^{-1}	Entropy of fusion

KLB-1 $T_{solidus}$, $T_{lhz\text{-}liq}$ and $T_{liquidus}$ from Katz et al. (2003). Unless otherwise indicated, other values are new, and for use with the equations of Katz *et al.* (2003).
*From Shorttle *et al.* (2014).